Department of Physics and Astronomy

Heidelberg University

Bachelor Thesis in Physics

submitted by

Stepan Kokh

born in Wuppertal (Germany)

2022

Pulse Characterization by Frequency-Resolved Optical Gating for Velocity Map Imaging of Xenon

This Bachelor Thesis has been carried out by Stepan Kokh at the
Max Planck Institute for Nuclear Physics in Heidelberg
under the supervision of
Apl. Prof. Dr. José Ramón Crespo López-Urrutia

Pulse Characterization by Frequency-Resolved Optical Gating for Velocity Map Imaging of Xenon

A velocity map imaging (VMI) setup, which will be applied in the future to studying low-intensity strong-field ionization and the nuclear transition of the ^{229m}Th isomer, is tested by multi-photon ionization (MPI) of xenon and the electron energy distribution is reconstructed. The ultra-short ionizing laser pulse of a 100 MHz frequency comb is characterized by second harmonic intensity frequency-resolved optical gating (FROG) and interferometric FROG (iFROG). A good agreement of both methods is found, and a pulse duration of 183 fs is retrieved. The peak intensity of the ionizing pulse during MPI is calculated from the measured intra-cavity power and the retrieved pulse shape, which allows a theoretical characterization of the MPI process and a comparison to the experimental results.

Pulscharakterisierung durch frequenzaufgelöste optische Verknüpfung für räumlich aufgelöste Geschwindigkeitsabbildung von Xenon.

Ein Aufbau für räumlich aufgelöste Geschwindigkeitsabbildung (VMI), der in Zukunft zur Untersuchung von Ionisation mit starken Feldern bei niedriger Intensität und des nuklearen Übergangs des ^{229m}Th Isomers angewandt wird, wird getestet durch multiphotonische Ionisation von Xenon und die Energieverteilung der Elektronen wird bestimmt. Der ultrakurze ionisierende Laserpuls eines 100 MHz Frequenzkamms wird charakterisiert durch frequenzverdoppelte Intensitäts frequenzaufgelöste optische Verknüpfung (FROG) und interferometrisches FROG (iFROG). Eine gute Übereinstimmung beider Methoden ist gefunden worden und eine Pulsdauer von 183 fs erhalten. Die maximale Intensität des ionisierenden Pulses bei multiphotonischer Ionisation wird berechnet aus der in der Kavität gemessenen Leistung und der bestimmten Pulsform. Dies erlaubt die theoretische Untersuchung der multiphotonischen Ionisation und den Vergleich mit den experimentellen Ergebnissen.

Contents

List of Figures

Chapter 1

Introduction

The measurement of the momentum distribution of photoelectrons allows the investigation of ionization processes and internal nuclear and electronic structures of atoms and molecules [1]. Velocity-map imaging (VMI) is a technique that permits the measurement of the momentum distribution of electrons or ions produced by ionization [2]. Simultaneous observation of kinetic energy and angular distribution of photoelectrons is a powerful tool to investigate strong-field light-matter interactions [3]. We plan to apply the VMI setup to study low-intensity strong-field ionization [4] and to probe the nuclear transition in ^{229}Th [5], which is considered a promising source for a new, more precise optical clock with inaccuracy in the range of 10^{-19} [6].

The general idea of a time reference is that a resonator oscillates with a known frequency f, which can be converted into a reference time T using the relation $f = \frac{1}{T}$. This value is then used as a reference point. The idea of Lord Kelvin in 1879 of using atomic transitions for referencing time [7] was the first step in producing an atomic clock. Today, many everyday objects such as GPS or time synchronization systems rely on atomic clocks [7]. Compared to other oscillators used for time reference, such as mechanical or electric oscillators, the advantage of an atomic clock is the reliability and reproducibility, achievable only in atomic systems [7]. In an atomic oscillator, the resonance frequency of an electron transition is used as a reference. Currently, most atomic clocks are based on cesium due to its heavy mass and the large transition frequency between its hyperfine states [7]. Specifically, in 1958 the atomic second was defined using the hyperfine transition of cesium as 9.192.631.770 cycles [8]. This definition holds until this day as the reference for the second.

One major disadvantage of atomic clocks is the sensitivity to external perturbations. The electromagnetic transitions of a nucleus could be used to overcome this. For most nuclei, the transition energies between excited states lie in the order of MeV due to strong binding energies [9]. An exception is the first excited state of thorium 229 (^{229m}Th) with a transition energy lying in the optical frequency range at approximately 8 eV [10], [11]. This property can be used by exciting the nucleus by nuclear excitation by electron transition (NEET) or a direct laser excitation, followed by a decay to the ground state, detectable by an electron bridge (EB) process [9] or internal conversion (IC) [10]. As theoretically described in [12], NEET leads to the ejection of an inner electron from the atomic shell, which causes the repopulation of the state by the jump of an adjacent shell electron into the vacancy. The difference in energy is generally released through the emission of a photon or an Auger process but can also cause a nuclear excitation. In an EB process, the deexcitation of the nucleus leads to the excitation transition of an electron, used to determine the excitation energy and lifetime of ^{229m}Th [13]. In highly charged ions (HCI) of thorium, which can be produced by an electron beam ion trap (EBIT), the fine structure splitting is large enough to be excited in an EB process [14]. For the spectroscopy of such states, a frequency comb can be applied. It is given by ultra short pulses with a fixed phase relation, producing a comb-like structure in the frequency domain. This is an advantage for spectroscopic experiments, which enables the absolute frequency of an electronic transition to be determined. For application to the high energy thorium transition, the comb needs to be transferred to the XUV range by high harmonic generation, yielding an XUV frequency comb [15], [16]. Alternatively, the deexcitation of the thorium nuclear state by IC can be used to determine the nuclear excitation energy by measuring the energy of the emitted electron. This decay channel of ^{229m}Th has a lifetime of $\sim$10 µs [10]. After emission, the electron energy distribution can be detected using the multi-channel plate (MCP) detector of a VMI setup.

VMI maps the electron momentum vector on the detector, regardless of the ionization position. A three-electrode system is used as an electrostatic lens to guide the electron through a time-of-flight tube onto a MCP detector. The impact position of the electrons on the detector surface is given by the projection of the electron momentum vector on the detector plane. From the resulting images, the electron energy distribution can be reconstructed. For a theoretical calculation of the electron energy distribution, the peak power of the ionizing laser needs to be determined based on the measured average power

and the pulse shape.

Generally, a reference shorter than the laser pulse is needed to determine the pulse shape. For pulses in the femtosecond range, such a reference is usually not available [17]. Therefore, frequency-resolved optical gating (FROG) may be implemented [18]. Specifically, instead of using a reference for the measured pulse, the pulse is referenced to itself. For this, the laser beam is split into two copies. One of them is delayed by a variable and precisely set delay stage. Then the pulses are recombined in a nonlinear crystal for second-harmonic generation [17]. A non-collinear and collinear alignment are used for intensity FROG and interferometric FROG (iFROG), respectively [19]. Measuring the spectrum of the second harmonic beam in dependence on the delay yields a FROG trace. It holds the information over the temporal and spectral pulse shape and phase, extractable with a numerical reconstruction algorithm.

In this thesis, both intensity and interferometric FROG are applied for ultrashort laser pulse characterization. At that, several noise reduction algorithms are implemented and compared. The retrieved pulse shape is used to test a VMI setup by multi-photon ionization of xenon. In the future, the setup will be applied to the nuclear transition of the ^{229m}Th isomer and the investigation of low-intensity ionization processes using VMI.

The thesis is structured as follows. The theoretical background for pulse characterization by FROG and iFROG and the measurement of multi-photon ionization by VMI is given in Chapter 2, followed by a description of the experimental setup in Chapter 3. In Chapter 4, the pulse shape is characterized by FROG and compared to the iFROG results in Chapter 5. With this knowledge, the MPI of xenon is theoretically and experimentally analyzed in Chapter 6, followed by a summary and conclusion in Chapter 7.

Chapter 2

Theoretical Background

This chapter gives a general theoretical basis of frequency comb lasers, their characterization, and their interaction with matter. First, a general introduction to non-linear optics and photoionization processes in high-intensity laser fields is given. Followed by a theoretical introduction of the FROG and iFROG technique. Finally, a brief insight into 3D reconstruction methods is provided.

2.1 Ultrashort Laser Pulses

Ultrashort laser pulses are widely used in modern physics as they provide a unique combination of short interaction time with matter and high peak intensity.

The electric field of a laser pulse can be written using a general wave function representation, as

$$\epsilon(z,t) = A(z,t)\exp(i(kz-\omega t)), \tag{2.1}$$

where A is the Amplitude, k and ω are the wave vector and frequency respectively. The intensity of the pulse is given by $I(z,t) = \left|\epsilon(z,t)^2\right|$. The main characteristic of a laser pulse is the complex amplitude, which in the time domain can be defined as [17]

$$E(t) = \frac{1}{2}\sqrt{I(t)}\exp(-i\varphi(t)), \tag{2.2}$$

with Intensity $I(t)$, time t and temporal phase $\varphi(t)$. By applying the Fourier transformation

$$\mathcal{F}(y) = \int f(x)\exp(-ixy)dx, \tag{2.3}$$

the complex amplitude is yielded as a function of the frequency

$$\tilde{E}(\omega) = \sqrt{S(\omega)}\exp(-i\phi(\omega)), \tag{2.4}$$

with the spectrum $S(\omega)$ and the spectral phase $\phi(\omega)$.

2.1.1 Self-Phase Modulation

For light passing through a medium, the refractive index can be defined as

$$n = \frac{c}{v}, \tag{2.5}$$

with the speed of light c and the phase velocity v in the medium. Since light can be described as an electromagnetic wave, the Kerr effect applies when calculating the refractive index for an intense beam. Discovered in 1875 by John Kerr [20], it describes the change of the refractive index n of a medium due to an external electric field of intensity I [21]

$$n(I) = n + n_2 I, \tag{2.6}$$

with the non-linear refractive index n_2. The corresponding phase shift of the light in a medium of length L is

$$\varphi(t) = -kn(I)L. \tag{2.7}$$

The nonlinear part is given as

$$\varphi_2(t) = -kn_2 I(t)L. \tag{2.8}$$

This phase shift broadens the pulse spectrum and is called self-phase modulation (SPM). The broadening of the pulse spectrum through SPM leads to a chirp, which describes the separation of frequencies in time. An increasing frequency in time is called an up-chirp, and a decreasing frequency a down-chirp.

2.1.2 Mode Locking

For most cases, it is sufficient if a laser emits a continuous wave of monochromatic light, limited only by the natural bandwidth of the electronic transition. The laser frequency is then defined by the gain medium used in the laser. For simplicity, a laser with a

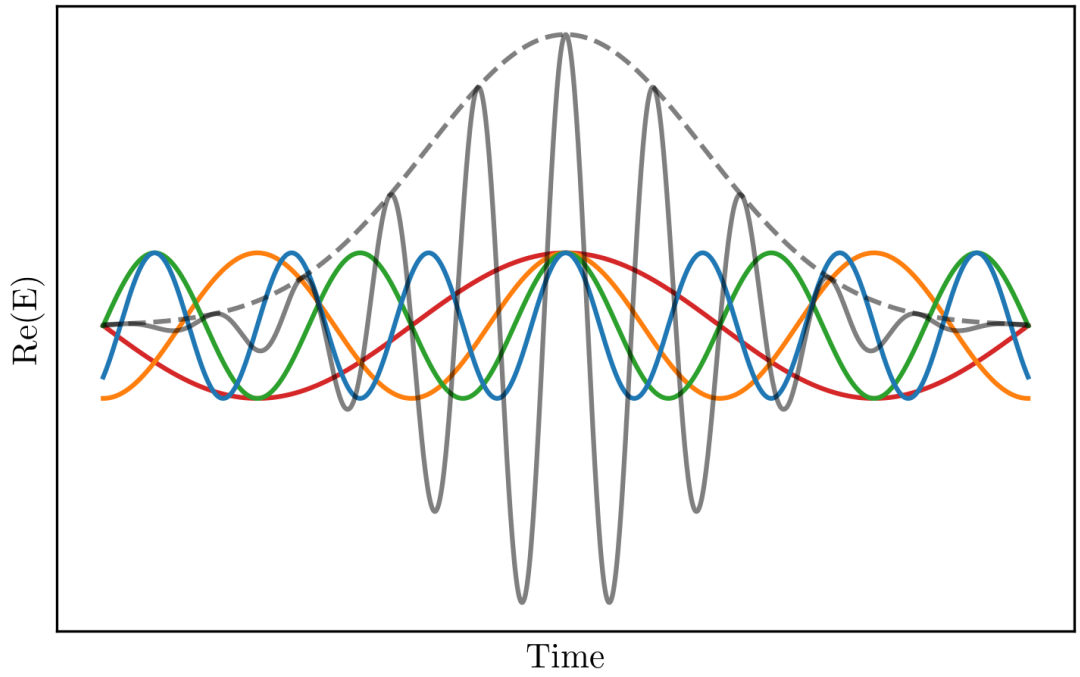

Figure 2.1: Schematic representation of mode-locking. The gray curve shows the interference of the real part of the four waves with different frequencies depicted in red, blue, green and yellow. The four waves have a fixed phase relation, thus leading to a stable Gaussian envelope, drawn as a dashed gray line. Adapted from [22].

gain medium inside a cavity consisting of two mirrors is considered in this section. The gain-bandwidth defines the spectrum of frequencies around the central frequency of the laser. If the distance between the cavity mirrors is a multiple of half the wavelength of the observed light, it produces a standing wave. Due to the gain bandwidth, multiple standing waves occur at different frequencies (referred to as the laser modes). The formation of a single pulse with a Gaussian shape by the interference of several waves with different frequencies is illustrated in Fig. 2.1. Following Heisenberg's uncertainty principle, to generate a short pulse length in the time domain, the pulse must be broad in the frequency domain, thus requiring many frequencies. The modes need to have a fixed phase relation to guarantee that simultaneously all modes interfere constructively and a pulse consisting of their frequencies is formed. Such a laser setup is called mode-locked.

2.1.3 Frequency Comb

The pulses of a laser with a stabilized mode-lock are emitted at a repetition rate f_{rep}, which depends on the round trip time of one oscillation $T_{\mathrm{rep}} = 1/f_{\mathrm{rep}}$. This results in a periodic pulse train with pulses separated by T_{rep}. The electric field of such a pulse

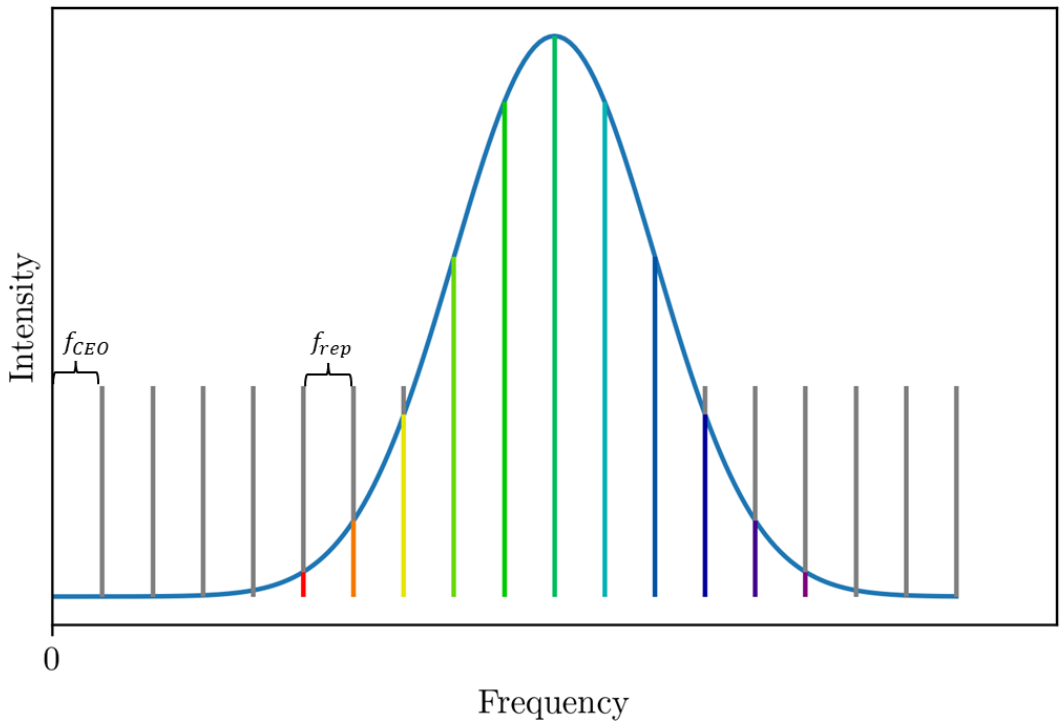

Figure 2.2: Schematic representation of a frequency comb. The different frequencies of the comb, shown by vertical lines in different colors, are modulated by the Gaussian envelope (shown in blue). The difference between the vertical lines is given by the repetition rate f_{rep}, and the shift of the first line from zero by the carrier-envelope offset f_{CEO}.

train with N pulses is the sum over the pulses

$$E_{\mathrm{train}}(t) = \sum_{n=0}^{N} A(t - nT_{\mathrm{rep}}) \exp\left(i(\omega_c t - n\omega_c T_{\mathrm{rep}} + n\Delta\varphi)\right), \tag{2.9}$$

with the Amplitude A, the central frequency ω_{c} and the fixed phase between pulses $\Delta\varphi$. As described in [22], the Fourier transform of this function yields a sum of Dirac distributions

$$\tilde{E}_{\mathrm{train}}(\omega) = \tilde{A}(\omega - \omega_c) \sum_{n=0}^{N} \delta\left(\omega T_{\mathrm{rep}} + n\Delta\varphi - 2N\pi\right), \tag{2.10}$$

which yields for $N \to \infty$ discrete frequencies, modulated by an amplitude function. This structure is called a frequency comb and is shown schematically in Fig. 2.2, with the vertical lines representing different frequencies of the comb, modulated by the Gaussian envelope. The phase difference $\Delta\varphi$ and repetition frequency f_{rep} result in the carrier-

envelope offset (CEO) for the zeroth frequency component

$$f_{\mathrm{CEO}} = \frac{\Delta\varphi}{2\pi} \cdot f_{\mathrm{rep}} = \frac{1}{T_{\mathrm{CEO}}}. \tag{2.11}$$

The repetition frequency corresponds to the distance between the lines in the frequency domain. Thus, the nth frequency can be calculated by

$$f_{\mathrm{n}} = f_{\mathrm{CEO}} + n f_{\mathrm{rep}}. \tag{2.12}$$

2.1.4 Optical Resonators

The simplest resonator cavity consists of two mirrors facing each other. One of them has a non-zero transmission for incoupling. The electric field inside such a cavity forms a standing wave that is defined in Ref. [23] as:

$$\begin{aligned} E_{\mathrm{c}}(\omega) &= E_{\mathrm{in}} t_{\mathrm{ic}} \left(1 + r_{\mathrm{ic}} r_{\mathrm{c}} e^{i\phi(\omega)} + \left(r_{\mathrm{ic}} r_{\mathrm{c}} e^{i\phi(\omega)}\right)^2 + \left(r_{\mathrm{ic}} r_{\mathrm{c}} e^{i\phi(\omega)}\right)^3 + ...\right) \\ &= E_{\mathrm{in}} t_{\mathrm{ic}} \sum_n \left(r_{\mathrm{ic}} r_{\mathrm{c}} e^{i\phi(\omega)}\right)^n \\ &= \frac{E_{\mathrm{in}} t_{\mathrm{ic}}}{1 - r_{\mathrm{ic}} r_c e^{i\phi(\omega)}}, \end{aligned} \tag{2.13}$$

where $t = \sqrt{T}$ denotes the transmission coefficient and $r = \sqrt{R}$ a reflection coefficient; T and R are the mirror reflectivity and transmission. The index ic denotes the input coupler, c the second mirror and E_{in} the input electric field. In deriving the last equation, the solution for the geometric series was used, since reflection and transmission coefficients are smaller or equal to one. $\phi(\omega)$ is the phase shift per roundtrip in the resonator, which depends on the frequency ω, the optical length of the resonator L, and the phase shift through dispersion $\phi_d(\omega)$ [24]

$$\phi(\omega) = \frac{\omega L}{c} + \phi_{\mathrm{d}}(\omega). \tag{2.14}$$

Without dispersion, the electric field inside the cavity is maximized by

$$\frac{\omega L}{c} = 2\pi n, \tag{2.15}$$

where n is an integer number. In the case of a frequency comb, resonance is achieved at a resonator length of [25]

$$L = \frac{c}{f_{\mathrm{rep}}}. \tag{2.16}$$

The amplification β of the electric field in a resonator cavity is given by the relation of the input intensity I_{c} and intra-cavity intensity I_{in}

$$\beta = \frac{I_{\mathrm{c}}}{I_{\mathrm{in}}} = \frac{t_{\mathrm{ic}}^2}{(1 - r_{\mathrm{ic}} r_{\mathrm{c}})^2}. \tag{2.17}$$

2.2 Second Harmonic Generation

If a classical system is assumed, the polarization of an electric field (laser) in a medium with susceptibility χ is expressed as

$$\vec{P} = \epsilon_0 \chi \vec{E}. \tag{2.18}$$

For an electric field in the range of the binding forces of the electrons to the atom, the electrons are forced out of their orbits. This introduces a non-linearity in the induced polarization, which can be written as a power series [26]

$$P_i = \chi_{\mathrm{ij}}^{(1)} E^j + \underbrace{\chi_{\mathrm{ijk}}^{(2)} E^j E^k}_{\text{second harmonic term}} + \chi_{\mathrm{ijkl}}^{(3)} E^j E^k E^l + \dots . \tag{2.19}$$

The second harmonic term can be interpreted as two photons of a frequency ω generating a photon of frequency 2ω, which is called second harmonic generation (SHG). Due to the phase conservation in this process, a coherent wave is emitted from the medium. Since the wave vector depends on the refractive index of the medium, the material in which the SHG takes place must have a regular structure. This condition is satisfied in crystals.

2.3 Photoionization

Instead of generation of scattered light, a laser beam can ionize the medium. There are several ways, in which the ionization can take place.

2.3.1 Photoelectric Effect

The photoelectric effect was first observed in 1839 by Alexandre Becquerel [27] while the theoretical interpretation was given by Albert Einstein in 1905 [28]. Einstein assumed that photons could be viewed as particles interacting with a medium and thereby ionizing an atom. This ionization process follows three general rules

1. Each chemical element is characterized by a specific ionization threshold; photons with energies below the threshold do not cause ionization.
2. The kinetic energy of photo electrons does not depend on the intensity of the light.
3. The number of photo electrons generated depends on the intensity.

The first two rules can be summarized in the formula for the kinetic energy of the photo electrons

$$E_{\mathrm{kin}} = \hbar\omega - I_{\mathrm{p}}, \tag{2.20}$$

where $\hbar\omega$ is the energy of a single photon with the frequency ω, $\hbar$ the reduced Planck constant, and I_p the ionization potential. If the energy of the photon is below the threshold given by the ionization potential, ionization is not possible. The ionization rate is given by

$$\Gamma = \sigma I, \tag{2.21}$$

where σ is the cross-section of the interaction and I is the laser intensity.

2.3.2 Multiphoton Ionization

The interaction of two photons was proposed in 1931 by Goeppert-Mayer [29] and later observed in transitions between Zeeman sublevels in atoms and molecules [30]. During multiphoton ionization (MPI), two or more photons interact to achieve in sum an energy larger than the ionization threshold. The requirement for this process is a strong laser intensity in the order of $>1 \times 10^{10}\,\mathrm{W\,cm^{-2}}$ since the ionization rate is proportional to the intensity to the power of the number of interacting photons N [30]

$$\Gamma = \sigma_{\mathrm{N}} I^N. \tag{2.22}$$

Here σ_{N} is the N-photon ionization cross-section. For ionization processes, it has to be differentiated between above-threshold ionization (ATI) and tunnel ionization. The idea

of tunnel ionization is that an electric field distorts the potential barrier of the atom, such that a finite possibility arises that a bound electron can tunnel through it. Under the conditions of an oscillating field, as in a laser beam, electrons may return due to the flip of the field after half a cycle and recombine with the atom. This phenomenon is used for high-harmonic generation.

2.3.3 Above-Threshold Ionization

ATI takes place if the summed energy of the absorbed photons is higher than the ionization potential. It was observed that an electron could absorb any number of photons P above the threshold and thus gain additional kinetic energy, corresponding to the total energy of the additional photons [30]. This yields discrete peaks in the kinetic energy of the resulting free electron given by

$$E_{\mathrm{kin}} = (N + P)\hbar\omega - I_{\mathrm{p}}. \tag{2.23}$$

In general, this is forbidden due to conservation of momentum, but if the electron is subjected to the field of a nearby atom, it may compensate the impulse with inverse bremsstrahlung [30]. Another characteristic of ATI is that the first peak, corresponding to a single photon absorbed above the threshold, gradually vanishes as intensity increases. This was explained by an increase in the ionization threshold resulting from the AC stark shift [30].

2.3.4 AC Stark Shift

The AC stark shift applies to electrons subjected to the oscillating electric field of a short laser pulse. They immediately oscillate at the laser frequency. Due to the oscillation, the electron acquires oscillation energy, also called the ponderomotive shift [4]

$$U_{\mathrm{p}} = \frac{e^2 E^2}{4 m_{\mathrm{e}} \omega^2}, \tag{2.24}$$

with the electron charge e and the electron mass m_{e}. The energy shift depends inverse quadratically on the laser frequency ω and is proportional to the square of the amplitude of the laser field E. Thus, for low intensities, the ponderomotive shift vanishes.

If the initial kinetic energy of the electron after ionization is smaller than the ponderomotive shift, the electron cannot escape the Coulomb field of the ion and thus is

preserved in a semi-bound state. Under these conditions, the electron is highly prone to absorption of photons and will escape the Coulomb field as soon as it has absorbed enough photons to reach a kinetic energy higher than the ponderomotive shift [30].

The inhomogeneity of the laser intensity in the focal spot produces a gradient of laser intensity for the electron after ionization. This interaction depends strongly on the time duration of the laser pulse. Since the ponderomotive shift depends on the laser intensity, in the case of pulses longer than 10 ps the electron is accelerated by the gradient and thus gains kinetic energy equal to the initial ponderomotive shift in the focus, while for short pulses this effect is negligible [30], [31].

For bound electrons, the effect of the ponderomotive shift depends on the state of the electron. While Rydberg states are significantly shifted to higher energy due to the oscillation, the effect on deeply bound states is lower and can most often be neglected. This difference in energy shifts yields the increase of the ionization potential by the ponderomotive shift [31]. The kinetic energy of an electron after ionization can therefore be calculated as

$$E_{\mathrm{kin}} = (N + P)\hbar\omega - I_{\mathrm{p}} - U_{\mathrm{p}}. \tag{2.25}$$

The energy shifts of xenon states are exemplarily shown in Fig. 2.3, where the energy of the states is shown as a function of the laser intensity. The energy levels of xenon are linearly shifted towards higher energies as laser intensity increases.

2.3.5 Freeman Resonances

Due to the ponderomotive shift, non-resonant states can be shifted into a multi-photon Freeman resonance [32]. This leads to a higher excitation probability at the corresponding laser intensity. This higher ionization probability can be seen as a fine structure in the resulting photoelectron energy spectrum.

2.3.6 Keldysh Parameter

To classify if an ionization process will happen due to MPI, or tunnel ionization, the Keldysh parameter γ can be used. Keldysh showed in 1965 that both mechanisms are based on the same process and proposed the Keldysh-parameter to classify which process

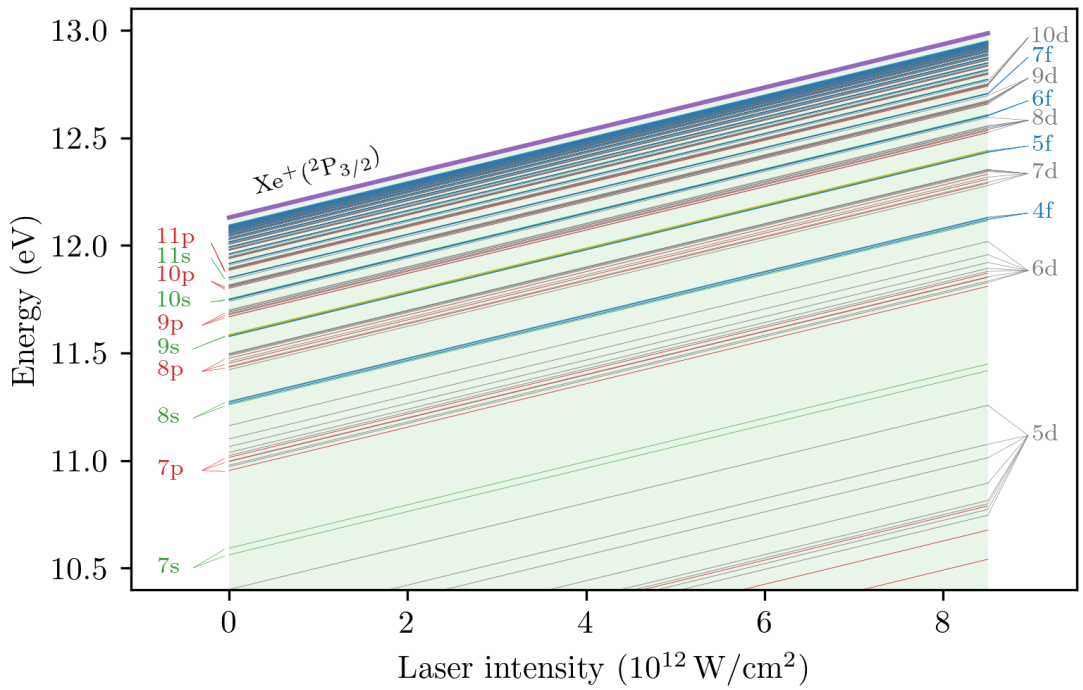

Figure 2.3: Shifting of xenon energy levels due to AC Stark shift, induced by a high-intensity laser. The energy of the levels is shown as a function of laser intensity, with the xenon energy levels marked by colored lines. The ionization potential is shown in purple. Adapted from [5].

takes place [33]

$$\gamma = \frac{\sqrt{2m_e\omega^2 I_p}}{eE}. \tag{2.26}$$

The parameter is $\gamma \gg 1$ for MPI and $\gamma \ll 1$ for tunnel ionization. With Eq. 2.24 it can be written with the ponderomotive shift as

$$\gamma = \sqrt{\frac{I_p}{2U_p}}. \tag{2.27}$$

2.3.7 Focal Averaging

The laser focus is another factor that influences the ionization process. Specifically, atoms at the edge of the focus interact with light of a different intensity, compared to the atoms in the center, due to the spatial spread of the laser intensity in the focus. This effect is called focal averaging [34]. The calculated electron energy distribution after MPI has to be corrected for this by weighing with the intensity distribution of the laser focus.

2.3.8 Central Limit Theorem

Multiple photons with different energies interact during a MPI process. The probability of a photon with specific energy interacting in such a process is given by the spectrum of the laser. The central limit theorem applies when variables are sampled from a distribution and added together, as in MPI. It states that the resulting distribution will converge for a large number of samples towards a Gaussian distribution [35].

2.4 Pulse Characterisation

The main focus of this thesis is the characterization of an ultra-short laser pulse. The first approach is autocorrelation, which will be described in the following. After that, FROG is described as an improved autocorrelation process, and alternative characterization methods are presented, such as d-scan or SPIDER.

2.4.1 Autocorrelation

In autocorrelation, a split-and-delay procedure is used to reference a laser pulse with itself. The schematic of an experimental setup for an autocorrelation measurement is shown in Fig. 2.4.

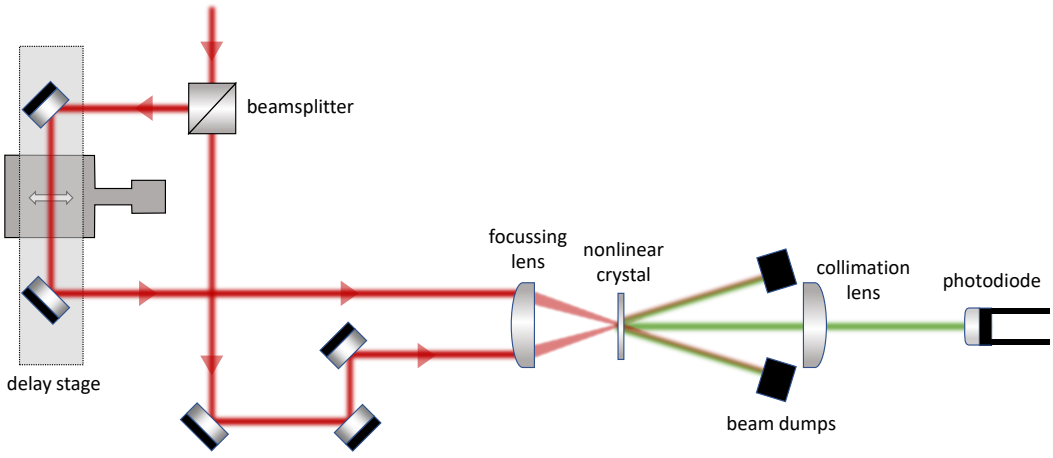

Figure 2.4: Schematic illustration of the autocorrelation setup. The beam is split using a beam splitter, and one part is delayed. Then, both beams are focused into a nonlinear crystal. The resulting SHG light intensity is measured using a photodiode.

The laser pulse is split into two identical pulses using a 50:50 beamsplitter. One of the resulting pulses propagates through an adjustable delay stage, while the other has a fixed beam path. Both pulses are then realigned and focused using a lens into a nonlinear crystal for SHG. A photodiode detects the resulting second harmonic light. Through variation of the path length Δs of the delayed laser beam, the delay τ can be changed by

$$\tau = \frac{\Delta s}{c}, \tag{2.28}$$

where c is the speed of light.
From Eq. 2.1 the resulting electric field can be derived to be the product of the original electric field $E(t)$ with the delayed field $E(t-\tau)$

$$E(t)_{\mathrm{SHG}} \propto E(t)E(t-\tau). \tag{2.29}$$

Since the photodiode is too slow to resolve the shape of a femtosecond laser pulse, the resulting signal $S(\tau)$ is the integral of the intensity over the duration of the pulse [17]

$$S(\tau) = \int I(t)I(t-\tau)dt, \tag{2.30}$$

with $E(t)^2 \propto I(t)$. The signal as a function of the delay yields the autocorrelation trace. It is important to remember that the signal is a convolution of two pulses, which results in a broadening of the trace's full width half maximum ($\mathrm{FWHM_{AC}}$) compared to the original pulse (FWHM). For a perfect Gaussian, the broadening is given by [22]

$$\mathrm{FWHM} = 0.7071 \cdot \mathrm{FWHM_{AC}}. \tag{2.31}$$

An autocorrelation measurement has some drawbacks. Due to the integration over the two overlapping pulses, the original pulse shape can not be retrieved unambiguously from the resulting structure. Also, the autocorrelation trace yields no information regarding the phase of the pulses.

2.4.2 Interferometric Autocorrelation

Instead of crossing the beams in the crystal in a non-collinear alignment, it is also possible to use a collinear alignment of the beams, as shown in Fig. 2.5.

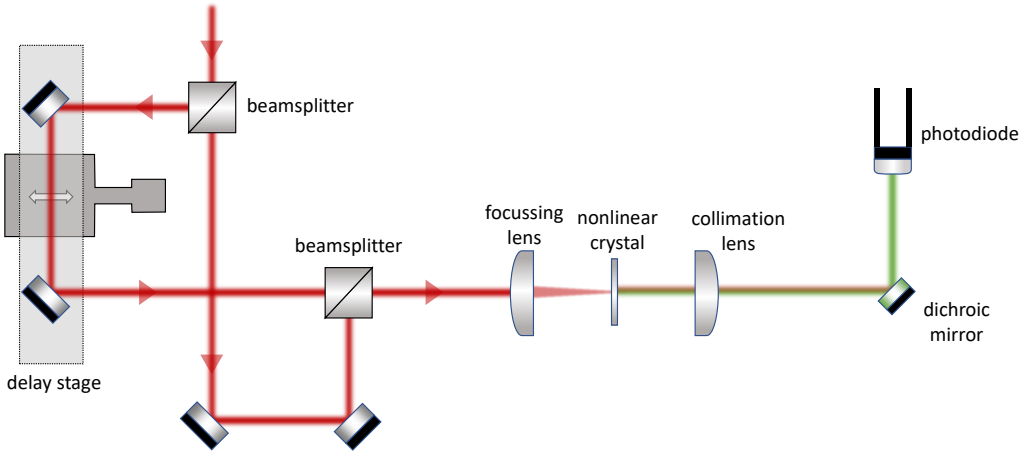

Figure 2.5: Schematic interferometric autocorrelation setup. The beam is split using a beam splitter, and one part is delayed. Then both beams are overlaid again before entering a nonlinear crystal. The resulting SHG light is filtered by a dichroic mirror and measured using a photodiode.

In this case, the beams are not crossed in the crystal but directed along the same path before entering the crystal. This leads to an interferometric interaction of the beams. Thus, the resulting SHG intensity depends on the intensities of the overlapping beams and their phase relation. If the beams are in phase, a maximum of intensity is measured by the photodiode, while half an optical cycle later, the beams are out of phase, and a minimum is measured. The result is interferometric fringes in the autocorrelation trace. Compared to intensity autocorrelation, the advantage of this method is a more straightforward alignment. Additionally, it enables the electric field, including the phase, to be retrieved from this trace [36]. However, the retrieval is not stable [17], so a better method is needed.

2.4.3 Frequency-Resolved Optical Gating

FROG uses the same initial experimental setup as autocorrelation, but the signal is obtained by spectrally resolving the SHG signal using a spectrometer instead of a photodiode. An example FROG trace of a 150 fs Gaussian pulse is plotted in Fig. 2.6. It is a two-dimensional image resulting from plotting the spectra (ordinate) as a function of the delay time (abscissa), with the intensity color-coded.

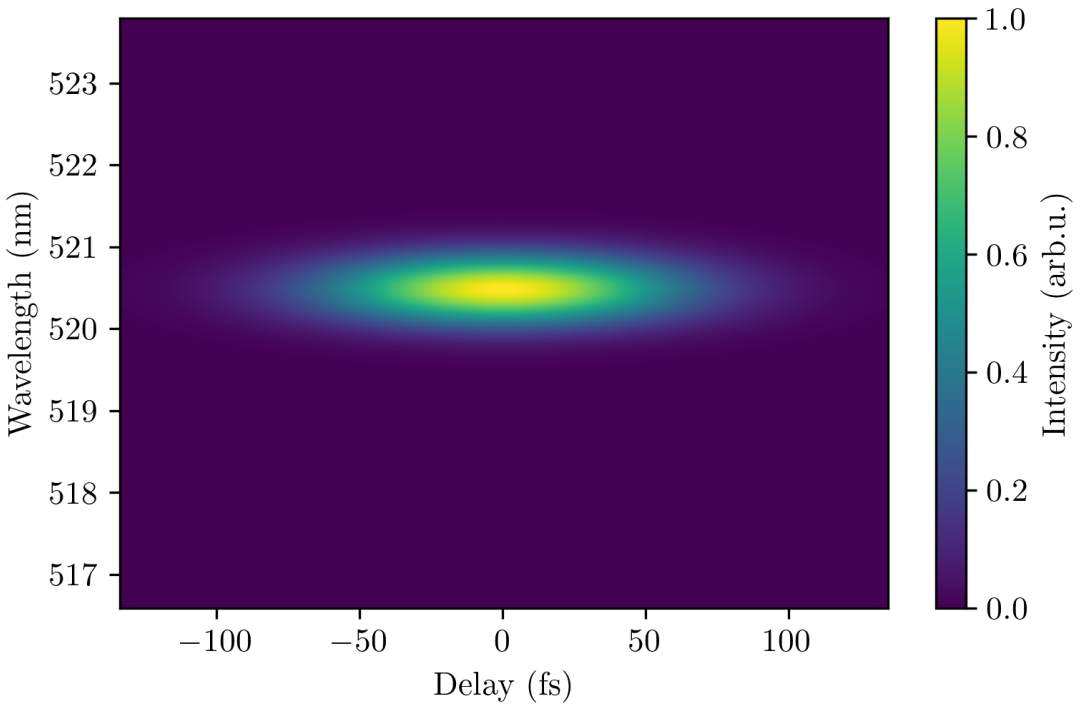

Figure 2.6: FROG trace of a Gaussian pulse of 150 fs width.

The trace contains the information about the laser pulse shape, as well as the phase of the pulse. The FROG trace $I_{\mathrm{FROG}}(\omega, \tau)$ can be easily generated from the electric field of the SHG pulse $E_{\mathrm{sig}} = E(t)E(t-\tau)$ by means of [17]

$$I_{\mathrm{FROG}}(\omega, \tau) = \left| \underbrace{\int E_{\mathrm{sig}}(t, \tau) \exp(-i\omega t) dt}_{\text{Fourier transform}} \right|^2 . \tag{2.32}$$

2.4.4 Retrieval from a FROG trace

Since the FROG trace results from the squared function of two variables (τ and ω), the inverse transformation from the trace to the electric field is non-trivial and poses the so-called two-dimensional phase-retrieval problem. An iterative retrieval algorithm is needed to retrieve the complex electric pulse from a FROG trace, as generally described in [17] and illustrated in Fig. 2.7. The algorithm is started with an initial guess of the electric field. A good first guess helps to speed up the retrieval process and improve the stability of the retrieval. In this work, the retrieval amplitude N-grid algorithm (RANA) approach, presented in [37], is used for the initial guess. For that, the spectrum is extracted from the measured FROG trace, and its Fourier transform is used as an

initial guess for the electric field $E^{(0)}(t)$. The iterative retrieval algorithm is a three-step process: (i) From the electric field, the signal field $E^{(0)}(t,\tau)$ is generated and Fourier transformed to get $E^{(0)}(\omega,\tau)$. (ii) $E^{(0)}(\omega,\tau)$ is compared to the measured FROG trace $I_{\mathrm{FROG}}(\omega,\tau)$, which should be proportional to the squared magnitude of $E^{(0)}(\omega,\tau)$ and $E^{(0)\prime}(\omega,\tau)$ is generated. (iii) After an inverse Fourier transform, the modified signal field $E^{(0)\prime}(t,\tau)$ is received, which is used to make a new guess for the electric field $E^{(1)}(t)$. This cycle is repeated until a suitable guess is reached. The method of generating a new guess depends on the used retrieval algorithm.

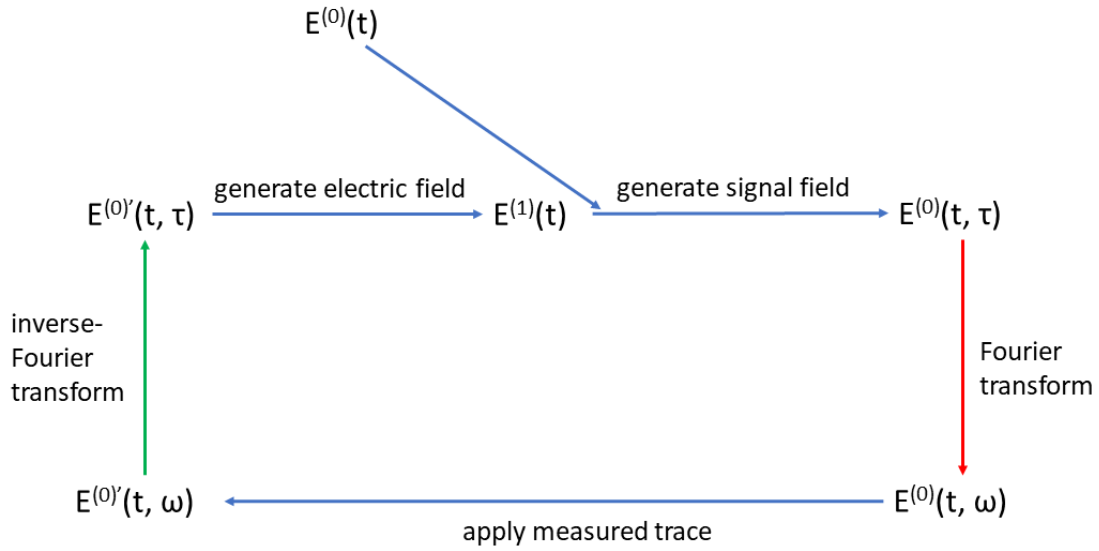

Figure 2.7: Schematic visualization of the general FROG retrieval algorithm.

Extended Ptychographical Iterative Engine

Two retrieval algorithms were evaluated on the measured data, the principal component generalized projections algorithm (PCGPA) [38] and the extended ptychographical iterative engine (ePIE) [39]. The latter one was shown to provide the best retrieval results for FROG and thus is used in the present study. The ePIE algorithm is implemented in Python, based on the recent publication by Sidorenko and coworkers [39].

At the beginning of each iteration i the current retrieved trace $I^i(\omega,\tau)$ is generated,

from the retrieved electric field $E^i(t)$ and the FROG error G calculated by

$$G = \sqrt{\frac{1}{N \cdot M} \cdot \sum_{n,m=0}^{N,M} \left| I_{\mathrm{nm}} - \left(\frac{\sum_{n,m=0}^{N,M} I_{\mathrm{nm}} \cdot I_{\mathrm{nm}}^{(i)}}{\sum_{n,m=0}^{N,M} {I_{\mathrm{nm}}^{(i)}}^2} \right) \cdot I_{\mathrm{nm}}^{(i)} \right|^2}, \tag{2.33}$$

with the original trace I and the indices n,m for the pixels of the FROG trace of size $N \times M$.

The delay τ can be written as $\tau = j\Delta t$, where Δt is the delay step, $j \in [1, J]$ the index of the delay axis and J the size of the delay axis. The columns are randomly rearranged for every iteration step, i.e., the index j is in random order. Every step, an internal loop over j generates a new guess for the electric field E^j. For that, the signal of the field $\psi_j(t)$ is calculated as

$$\psi_j(t) = E^{(j)}(t) E^{(j)}(t - j\Delta t) \tag{2.34}$$

and, after Fourier transformation

$$\psi_j(\omega) = \mathcal{F}(\psi_j(t)). \tag{2.35}$$

The Fourier transformed signal is normalized and multiplied with the square root of the spectrum of the FROG trace at the jth delay step

$$\psi_{\mathrm{j}}(\omega) = \sqrt{I_j(\omega)} \frac{\psi_j(\omega)}{|\psi_j(\omega)|}. \tag{2.36}$$

The updated signal is then calculated by an inverse Fourier transform

$$\psi_j'(t) = \mathcal{F}^{-1}(\psi_j(\omega)). \tag{2.37}$$

Finally, the updated electric field is calculated by

$$E^{(j+1)}(t) = E^{(j)}(t) + \alpha \frac{{E^{(j)}}^*(t - j\Delta t)}{\left|E^{(j)}(t - j\Delta t)\right|^2_{\max}} \cdot \left(\psi_j'(t) - \psi_j(t)\right), \tag{2.38}$$

with a uniformly distributed parameter $\alpha \in [0.1, 0.5]$, which controls the strength of the update (* denotes the complex conjugate). Smaller α require more steps to reach

convergence. However, if α is too large, the iteration could skip the global minimum. After the internal loop is run for every j, the next iteration $i+1$ is started by calculating the retrieved trace. The iterations continue until a stopping criterion is reached. This can be a duration in seconds, the number of iterations, the number of iterations without improvement, or if a FROG error is reached.

2.4.5 Interferometric Frequency-Resolved Optical Gating

Just like interferometric autocorrelation is an alternative method to set up an autocorrelation measurement, interferometric FROG (iFROG) can be used instead of FROG. For this, the interferometric autocorrelation setup is used, together with a spectrometer, which yields an iFROG trace illustrated in Fig. 2.8 (c) for a 150 fs Gaussian pulse. The corresponding autocorrelation, gained by integrating over the spectra, is presented in Fig. 2.8 (a). For a pulse with the complex electric field

$$\epsilon(t) = E(t)\exp(i\omega_0 t), \tag{2.39}$$

the resulting iFROG trace is given by [40]

$$I_{\mathrm{FROG}}(\omega,\tau) = \left| \int \left(\epsilon(t) + \epsilon(t-\tau)\right)^2 \exp(-i\omega t) dt \right|^2 . \tag{2.40}$$

The trace contains several modulation components B_n, that can be analytically separated. Defining $\Delta\omega = \omega - 2\omega_0$, these components can be represented as [41]

$$B_0 = 2\left|E_{\mathrm{SHG}}(\Delta\omega)\right|^2 + 4\left|E_{\mathrm{FROG}}(\Delta\omega,\tau)\right|^2 , \tag{2.41}$$

$$B_1 = 8\left|E_{\mathrm{SHG}}(\Delta\omega)E^*_{\mathrm{FROG}}(\Delta\omega,\tau)\right|^2 \cdot \cos\left(\phi_{\mathrm{SHG}}(\Delta\omega) - \phi_{\mathrm{FROG}}(\Delta\omega,\tau) - \frac{\Delta\omega\tau}{2}\right) \tag{2.42}$$

and

$$B_2 = 2|E_{\mathrm{SH}}(\Delta\omega)|, \tag{2.43}$$

where ϕ_i is the phase of the complex field trace E_i.

$$E_{\mathrm{SHG}} = \int E^2(t)\exp(-i\Delta\omega t) dt \tag{2.44}$$

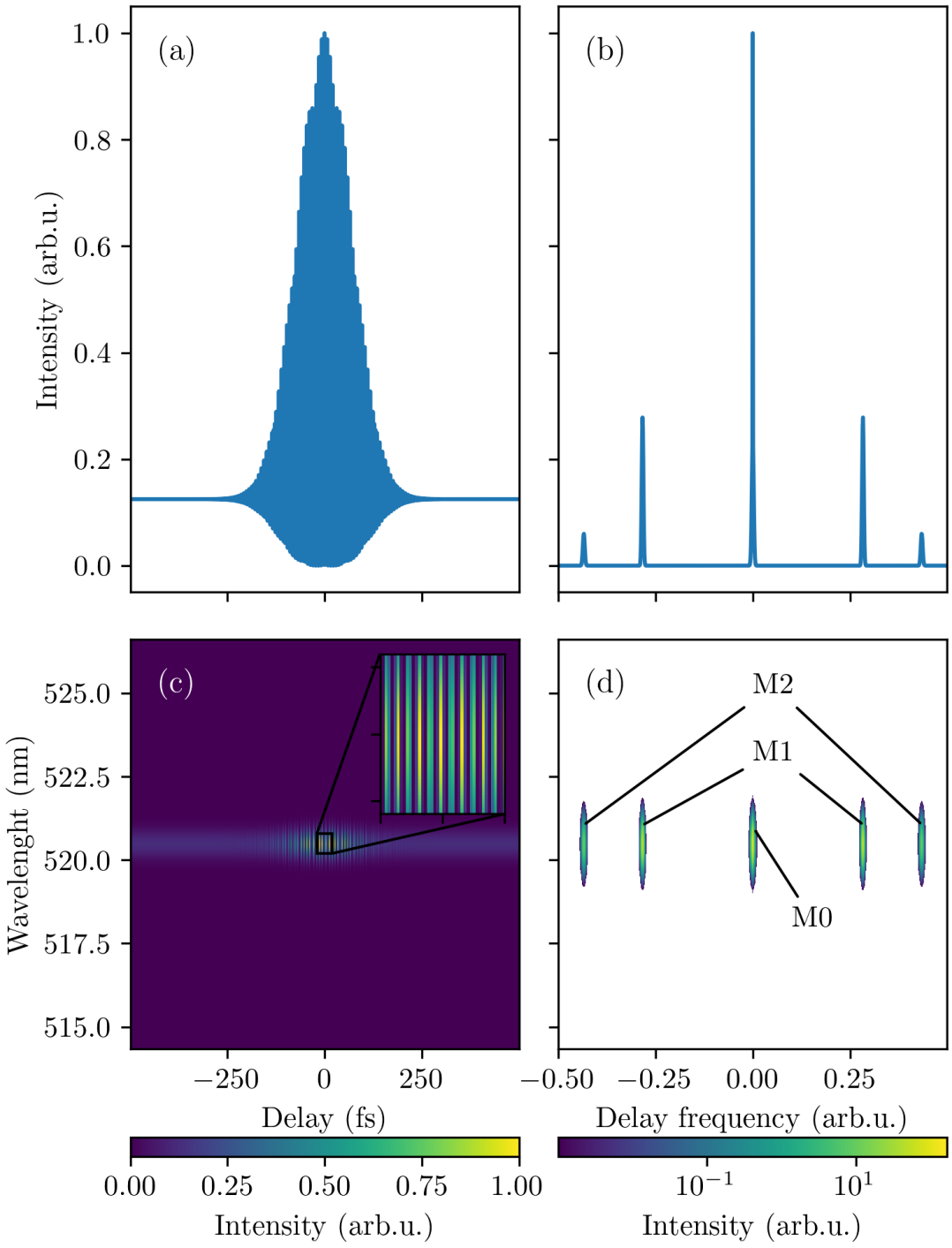

Figure 2.8: Fourier analysis of theoretical Gaussian iFROG trace. (a) Autocorrelation of (c) achieved by integrating over the spectra. The intensity is normalized to one. (b) Horizontal slice taken from (d) at the central wavelength of 520 nm. (c) Trace of a theoretical Gaussian pulse with a width of 150 fs. The inset shows a zoom of the central part. (d) The image gained from (c), by using a one-dimensional Fourier transformation of the delay axis, plotted in logarithmic scale. M0, M1, and M2 are the modulation bands of (c).

is the electric field of the SHG of a single pulse, which is independent of the delay and is visible as the constant background line in Fig. 2.8 (c).

$$E_{\mathrm{FROG}} = \int E(t)E(t-\tau)\exp(-i\Delta\omega t)dt \tag{2.45}$$

is the standard intensity FROG trace. From the modulation components, the modulation bands M_n are gained by

$$M_n = B_n \cos\left[n\left(\omega_0 + \frac{\Delta\omega}{2}\right)\tau\right]. \tag{2.46}$$

M_n are the subtraces of the iFROG trace, which are visualized in logarithmic scale in Fig. 2.8 (d) by Fourier transformation along the delay axis of the iFROG trace. Due to the symmetry of the Fourier transformation, the two modulation components are visible to the left and right of the dc band. The horizontal slice at the central wavelength is shown in Fig. 2.8 (b). M_0 corresponds to the dc band of the trace and can be obtained using a low pass filter. The result is shown in Fig. 2.9. In Fig. 2.9 (c) only the FROG trace is visible with the delay-independent background. This is especially evident in the autocorrelation shown in Fig. 2.9 (a), which shows a Gaussian pulse, elevated from zero by the background. In Fig. 2.9 (d) and Fig. 2.9 (b) only the dc-component is visible.

Eq. 2.41 shows that the FROG trace can be retrieved from this trace by subtracting the delay independent E_{SHG}, which can be acquired from the trace at high or low delays. The resulting FROG trace is shown in 2.10 and can be used for retrieval with a standard FROG retrieval algorithm, as described above.

2.4.6 Alternatives to FROG

FROG is not the only method for pulse characterization in the ultra-short range. Spectral phase interferometry for direct electric-field reconstruction (SPIDER) was introduced as a faster and computationally cheaper characterization method in the 1990s by Iaconis and Walmsley [42]. In this method, an interferogram is measured for every delay step using a similar split and delay method as in FROG. Additionally, one of the sub-pulses is also shifted in frequency. For that, a stretched version of the pulse is produced and chirped to separate the frequencies temporally. Due to the chirp, it is possible to take two different temporal slices and mix them with the two test pulses to generate two frequency-shifted pulses. For the retrieval, the pulse is Fourier trans-

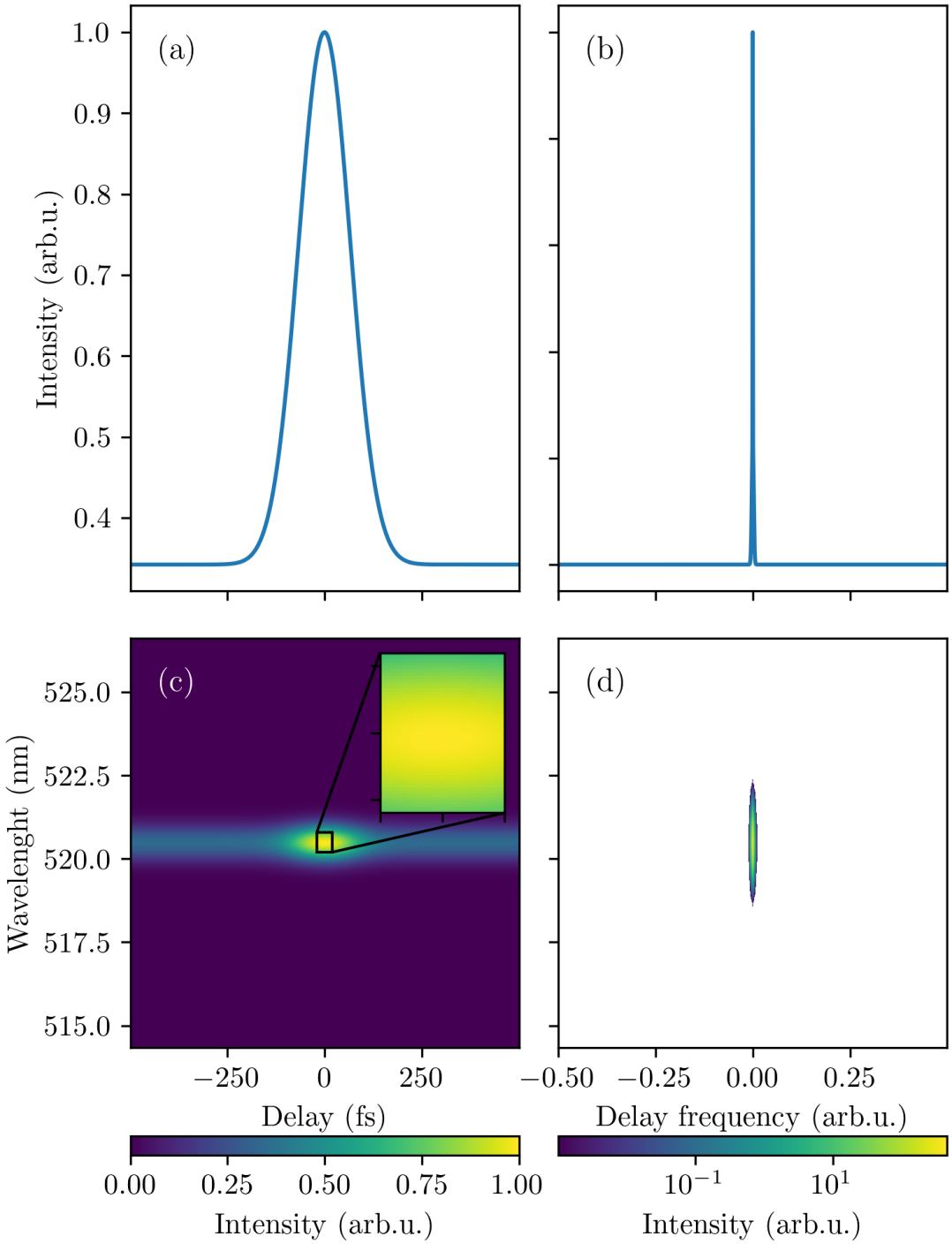

Figure 2.9: Fourier analysis of the low pass filtered pulse from Fig. 2.8 (c) as in Fig. 2.8. In (a) and (c) the oscillations are missing compared to 2.8 (a) and (c). (d) and (b) are missing high frequency features compared to 2.8 (d) and (b).

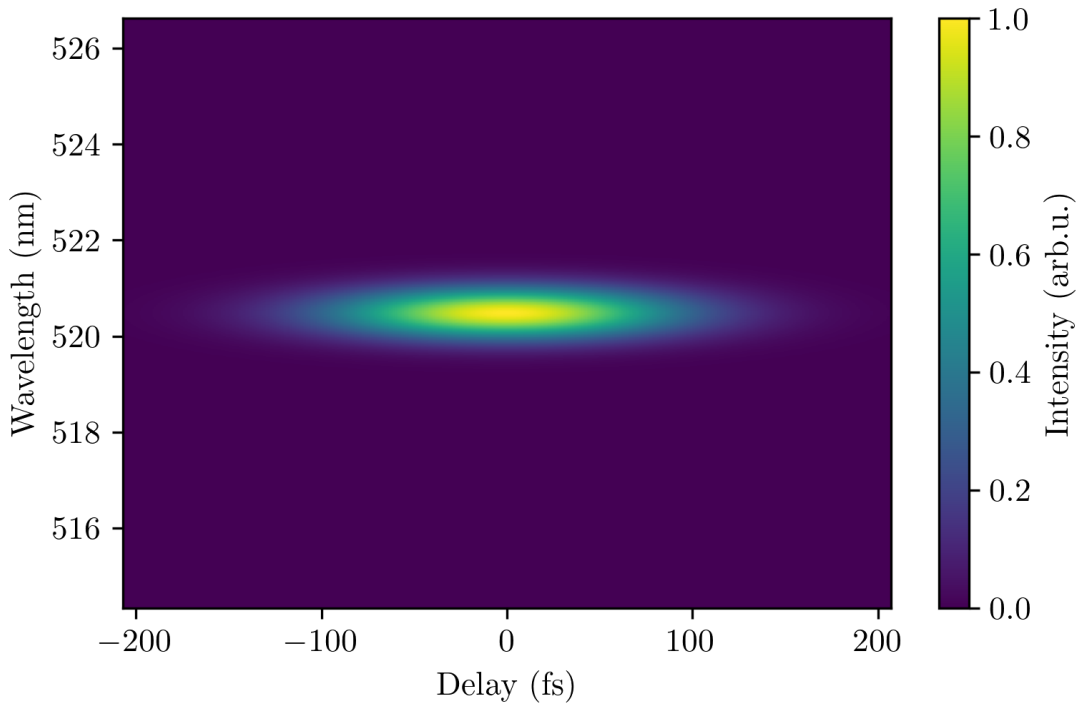

Figure 2.10: FROG trace gained from Fig.2.8 (c) using a low pass filter and background subtraction.

formed, and all the components, but the component at delay τ are filtered. The signal is then inverse Fourier transformed, and the phase is reconstructed by concatenating the resulting signals for the different delays. This method does not use an iterative reconstruction algorithm and is therefore faster. However, it needs a calibration measurement and careful implementation to avoid a frequent recalibration of the setup [17].

Another pulse characterization method is dispersion scan (d-scan) introduced by Miranda et al. in 2012 [43]. The experimental setup consists of a transparent glass plate, a SHG crystal, and a spectrometer. The d-scan trace is measured by varying the width of the glass insertion (i.e., the chirp of the pulse) and recording the pulse spectrum. In this case, the trace is the spectrum as a function of glass thickness. The pulse characteristics can then be retrieved using an iterative numerical algorithm similar to FROG.

2.5 Reconstruction methods of 3D distributions from 2D images

Due to experimental limitations, it is often difficult to measure a three-dimensional distribution directly. Thus, a two-dimensional projection of the distribution is usually measured, and then the original image is computationally reconstructed. This thesis considers two computational approaches that can be used for this purpose.

2.5.1 Abel Inversion

If a cylindrical symmetry and a symmetry axis parallel to the detector plane can be assumed for the measured distribution, the Abel transform may be used. For a function $f(r,z)$, it is given by [44]

$$F(y,z) = 2\int_{y}^{\infty} \frac{f(r,z)r}{\sqrt{r^2-y^2}}dr \tag{2.47}$$

and the inverse Abel transform by

$$f(r,z) = -\frac{1}{\pi}\int_{r}^{\infty} \frac{dF}{dy}\frac{1}{\sqrt{y^2-r^2}}dy. \tag{2.48}$$

Hereby, $f(r,z)$ is the 3D distribution, with the coordinates r and z. The projection on a 2D plane $F(y,z)$, with the coordinates y and z, is obtained through the forward Abel transform. The inverse Abel transform thus provides a 3D distribution from the projection. The forward Abel transform can be associated with measuring a 3D distribution using a 2D detector. The process is illustrated in Fig. 2.11.

2.5.2 Tomographic Reconstruction

Another method to reconstruct a distribution from a projection is tomography. The general idea of tomography is to use projections for different angles measured by either rotation of the object or the detector around the object. The 3D distribution can then be reconstructed from the measured projections, as described in [46]. This is a well-known process in medicine, used for magnetic resonance imaging and computer tomography scans.

The projections, obtained by the measurement at every angle, are called Radon transform, and the set of these projections for all angles can be visualized as a sino-

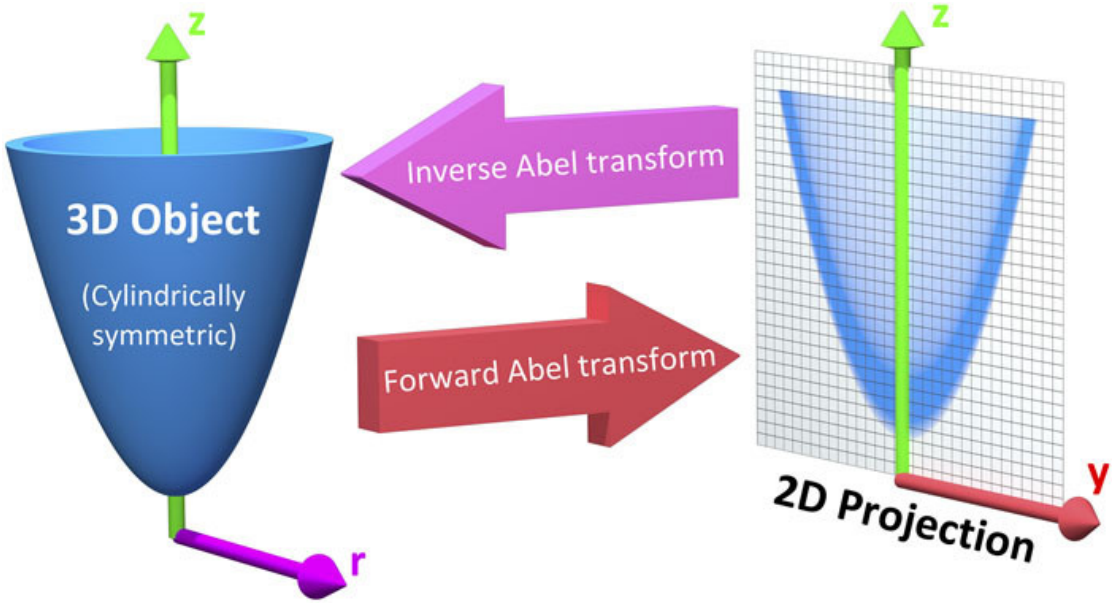

Figure 2.11: Visualization of Abel transform. Reproduced with permission from Review of Scientific Instruments 90, 065115 (2019). Copyright 2019, AIP Publishing [45].

gram. Then the Fourier-slice-theorem can be used to reconstruct the distribution from the projections. In 2D, it states that the 1D-Fourier transform of a projection can be identified with a slice through the origin of the 2D-Fourier transform of the original distribution. The original distribution can be reconstructed, by first, Fourier transforming the Radon transform, then applying the Fourier-slice theorem to arrange the projections, and finally, by inverse Fourier transforming the resulting image to obtain the original distribution. This method holds for N-dimensional distributions as well.

Chapter 3

Experimental Setup

This chapter presents the experimental setup used to retrieve the measurements later discussed in Chapters 3, 4, and 5. Specifically, the employed laser system and the FROG and iFROG setup are discussed. Finally, a VMI setup is introduced.

3.1 Laser System

In the reported experiments, a commercially available frequency comb FC1000-250 from Menlo Systems GmbH is used. It consists of a Yb- based fiber oscillator with a central frequency of 1039 nm, a spectral width of 7 nm and a repetition rate f_{rep} of 100 MHz. The outgoing light is stretched in 60 m of passive fiber to 24 ps. The average achieved power is 15 W. The resulting pulse can either be compressed internally by a grism-compressor [47] to 170 fs at 12 W of power or is coupled out. The beam is further amplified using an 80 cm long Yb-doped rod-type photonic crystal fiber amplifier and then compressed using a home-built grating compressor. The resulting beam has an average power of 80 W. Before it is used for further experiments, the pulse shape and length are characterized.

3.2 Pulse Characterization

In this thesis, the pulse characterization is done twice: once by FROG and once by iFROG. As both techniques are very similar, the same general setup is used for both measurements, modified only by replacing one component.

3.2.1 FROG Setup

As described in the previous chapter, for pulse characterization with FROG, the beam has to be split, delayed, joined again in a home-built autocorrelation system, and then measured using a spectrometer. The pulse characterization setup is shown in Fig. 3.1, with the autocorrelation setup on the left and the spectrometer on the right.

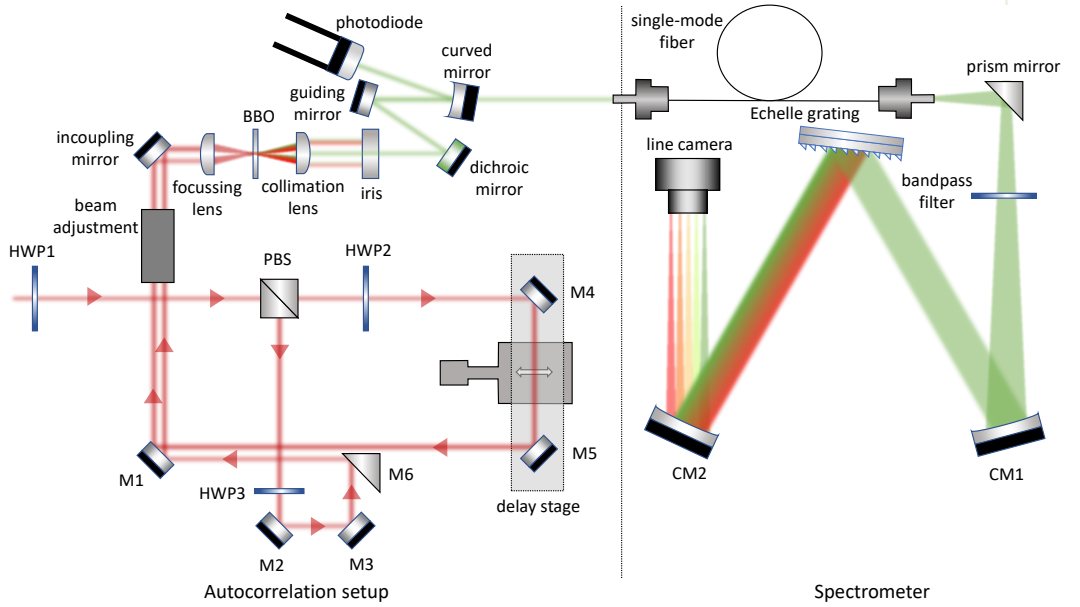

Figure 3.1: (Left) Delay stage for intensity autocorrelation. The pulse enters through the half-wave plate (HWP1) and is then split by the polarizing beam splitter (PBS). The polarization is again adjusted using HWP2 and HWP3. One pulse is delayed using a delay stage with two mirrors, M4 and M5. The other pulse follows along a path with two mirrors, M2 and M3, and a prism-mirror M6. Both pulses are coupled out with mirror M1. After beam adjustment, the beams enter the SHG stage, are focused into a BBO crystal, and then filtered using an iris. The SHG light is either detected by a photodiode or transferred to the fiber-coupled spectrometer. (Right) Spectrometer setup consists of a Czerny-Turner spectrometer using two curved mirrors and an Echelle grating, focusing the spectrally resolved light on a line camera.

The beam enters the delay-box through a rotatable half-wave plate (HWP1) and is then split into two identical beams using a polarizing beam splitter (PBS). Each beam follows one arm of the experiment. The wave plate through which the beam enters the box can thus be used to adjust the power in each arm. A second HWP (HWP1 and HWP2) is installed to rotate the beam polarization in each path. One of the pulses is delayed using a retroreflector consisting of two mirrors mounted on a moveable stage, with a maximal movement range of 20 mm and a minimum step size of 10 nm. Thus, the maximal range of delay is 133 ps and the minimal delay step is 0.067 fs. The second pulse

is guided by two mirrors, M2 and M3, and a prism-shaped mirror, M6, which allows the alignment of the beams. The parallel beams are guided out of the autocorrelation box using another mirror, M1. Using two individual mirrors for each beam on a home-built mount ensures that the beams are parallel. Upon entrance to the SHG stage, the beams are guided onto a lens using a mirror. The lens focuses the beams into a rotatable beta barium borate (BBO) crystal, used for SHG. The light is then collimated by means of a second lens. The SHG beam is further led through an iris diaphragm, and the part of the beam that corresponds to the second harmonic, generated by the individual uncorrelated pulses, is cut away. Further, the second harmonic, used for FROG measurements, is filtered using a dichroic mirror. Here, a curved mirror can be placed to reflect the light onto a photodiode, employed for an autocorrelation measurement.

Spectrometer

In the FROG measurements, the light is coupled into a home-built Czerny-Turner spectrometer, shown on the right of Fig. 3.1, using a single-mode fiber. In the spectrometer, a prism mirror guides the beam through a bandpass filter for green wavelengths, with the central wavelength at 520 nm and a bandwidth of 40 nm. Since the laser emits a pulse with a central wavelength of 1039 nm, the expected wavelength after the SHG crystal is ∼520 nm. The filtered light is then collimated and redirected onto an Echelle grating using a curved mirror CM1. The Echelle grating spectrally resolves the light, which is then collimated again by a curved mirror CM2. This mirror focuses every monochromatic beam onto a different position of the line camera with 2048 pixels that records the resulting spectrum. Through a calibration measurement with a Fe-Ne lamp, as described in [22], the wavelength is identified as a function of the pixel position px as

$$\lambda = \frac{-1.909 \cdot 10^{-7}}{px^2}\mathrm{nm}^2 + \frac{8.352 \cdot 10^{-3}}{px}\mathrm{nm} + 513.7\mathrm{nm} \tag{3.1}$$

3.2.2 Interferometric FROG Setup

Instead of using an autocorrelation setup, interferometric autocorrelation can be used to perform an iFROG measurement, as described in the previous chapter. The used setup is shown in Fig. 3.2.

It is similar to the setup for intensity autocorrelation presented in Fig. 3.1, except that instead of the prism mirror M6, which was used to bring both beams on a parallel path,

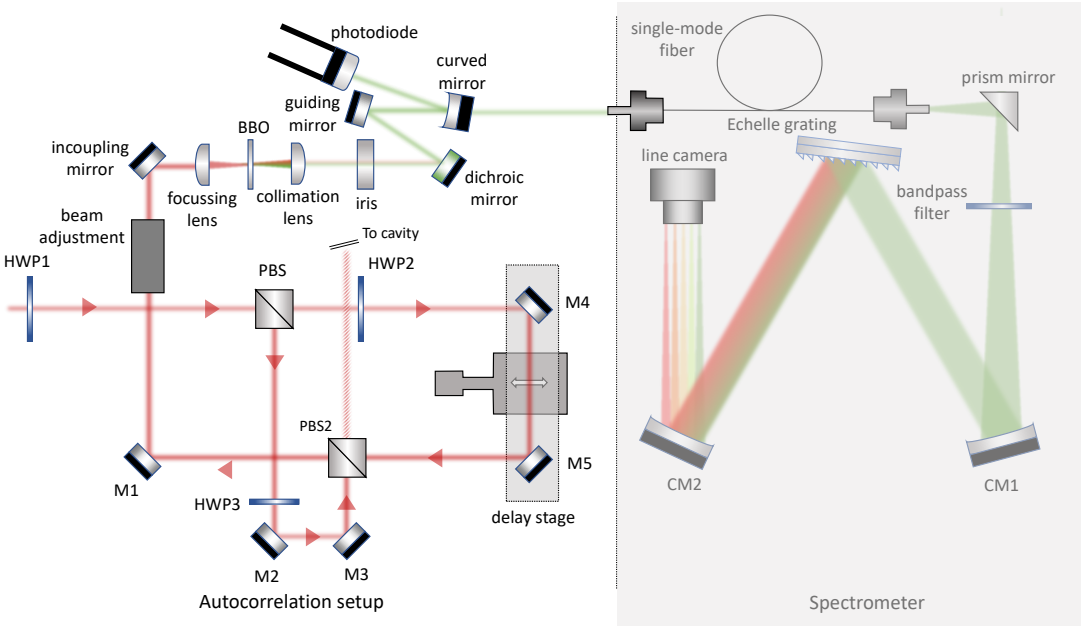

Figure 3.2: (Left) Delay stage for interferometric autocorrelation. The beam path for both pulses is identical as in Fig. 3.1, except for the alignment. Instead of prism mirror M6, a second polarizing beam splitter (PBS2) is placed at the intersection of both beam paths. (Right) Spectrometer setup as described in Fig. 3.1.

a second polarizing beam splitter (PBS2) is placed in the intersection of the two beam paths. Thus, the beam is split between the cavity and the SHG stage. The advantage of this setup is that the delay stage might also be employed for other experiments without any change in the experimental setup. HWP2 and HWP3 allow adjusting the light ratio directed to the cavity or the SHG stage. The beam adjustment and SHG-stage are the same as in intensity autocorrelation regarding optical components. Here, only one beam instead of two is focused in the BBO crystal. The beam can be measured using a photodiode or a spectrometer, which is identical to intensity FROG.

3.3 Velocity Map Imaging

Due to the high laser intensities needed for MPI, the VMI setup is built inside an enhancement cavity. The setup is tested by measuring the resulting photoelectron energy spectrum from MPI of xenon, which was chosen due to its low ionization potential.

3.3.1 Electrode setup

The measurement of an ATI process is done by focusing a high-intensity laser on a gas cloud, which leads to an ionization process. Electrons or ions are collected by an electric

field and detected using a microchannel plate (MCP).

This measurement method poses the problem that ionization products are generated in different locations. This results in distorted images due to smearing. To solve this problem, Eppink and Parker developed the VMI method in 1997. In VMI, electrostatic lenses are used to map charged particles on a detector insensitive to the initial position.

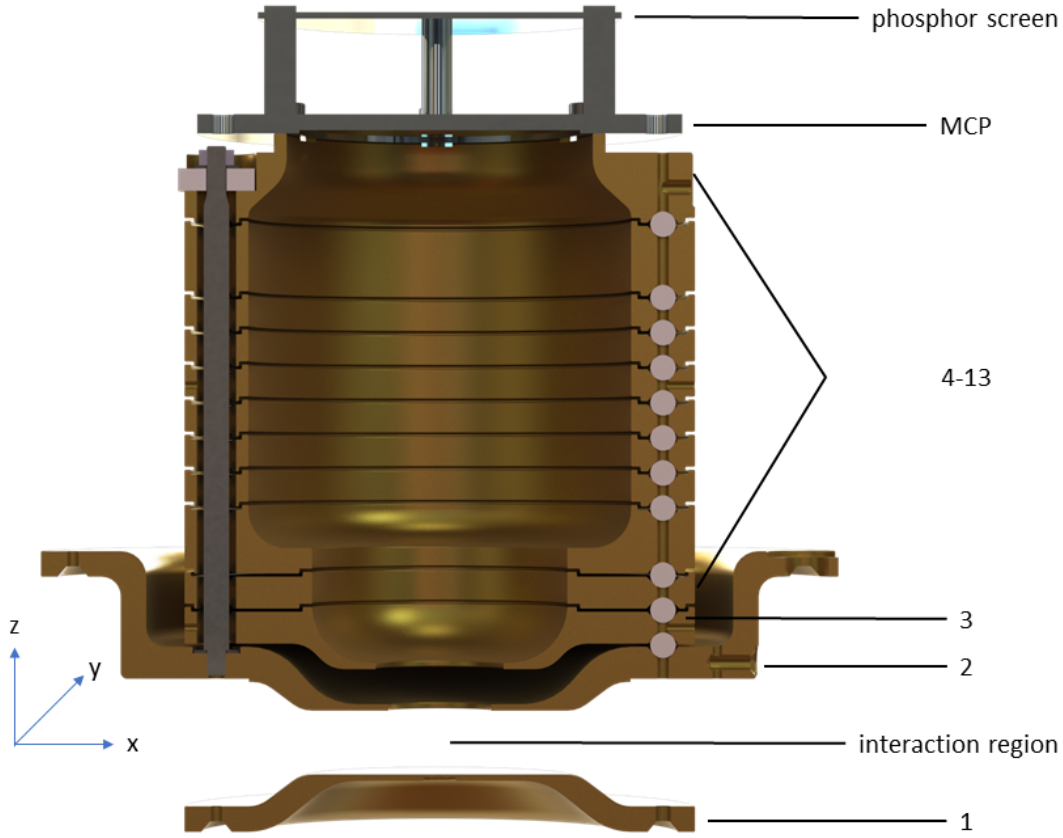

Figure 3.3: Section view of the VMI spectrometer used in this experiment. The electrode setup consists of 1. Repeller, 2. Extractor, 3. Ground and a TOF tube consisting of electrodes 4-13. The interaction region is between the repeller and extractor. The laser enters the setup in x direction. The gas is injected through a nozzle in the repeller electrode. The generated electrons are recorded using a MCP and a phosphor screen.

The VMI setup used in the experiment is presented in Fig. 3.3. The laser beam enters the setup in x direction and interacts with xenon gas in the interaction region between the repeller and extractor electrodes. The laser is enhanced in a femtosecond enhancement cavity (fsEC) that is described later. Xenon is injected through a nozzle in the repeller electrode. The laser ionizes the xenon due to MPI and the repeller accelerates the resulting photoelectrons towards the detector. The electrode configuration acts as

electrostatic lenses, which project the 3D electron distribution on the detector plane, independent of the position of the mother atom during the ionization. Combined with the time-of-flight (TOF) tube, this also guarantees that particles with the same charge to mass ratio reach the detector simultaneously. This is only relevant if ions are measured.

Additionally, the tube acts as a shield against external fields. The electrode design was chosen so that the electrodes intertwine to avoid penetrating external electromagnetic fields. The electrodes are supported on spheres in three positions and pressed together by three rods. The measurement is obtained with a camera recording the phosphor screen. The configuration of the electrode voltages is described in [25]. In a VMI measurement, the generated electron distribution is projected onto the 2D detector. The distribution is oriented in the laser polarization direction and depends on the state of the ionized electron. A structure of several rings is expected, directly correlating to the number of absorbed photons above the ionization threshold. Thus, the energetic difference between two adjacent rings is exactly one photon energy.

3.3.2 Femtosecond Enhancement Cavity

Since the probability of MPI scales with the laser intensity to the power of the number of absorbed photons, a significant increase in laser power is required to perform VMI measurements with xenon. To ensure this, a fsEC is installed as shown in Fig. 3.4, which enables reaching peak powers of $7.7 \cdot 10^{12}\,\mathrm{Wcm}^{-2}$.

The beam enters through a rotatable waveplate, used to control the polarization of the laser for the VMI measurement. The pulse is reflected using the plane mirror (M1) onto the input coupler (IC), which has a finite transmittance for the employed laser wavelength. M4 reflects the laser onto the curved mirror CM1. CM1 and CM2 focus the laser at the position of the VMI. M3 reflects the laser onto a piezo-mounted mirror (M5) connected to a movable piezo stage, which enables the variation of the optical length of the cavity. The cavity length is set to the resonance length of the laser, which is 3 m [24]. The adjustable mirror reflects the light onto the input coupler to complete one roundtrip.

This work uses two methods to achieve a reliable peak laser power in the cavity. The first one is to use the mirror mounted on the movable piezo stage to adjust the cavity length periodically. In this setup, the laser power oscillates between being resonant at the peak power and falling out of resonance, as illustrated in Fig. 3.5 (a). The plot shows

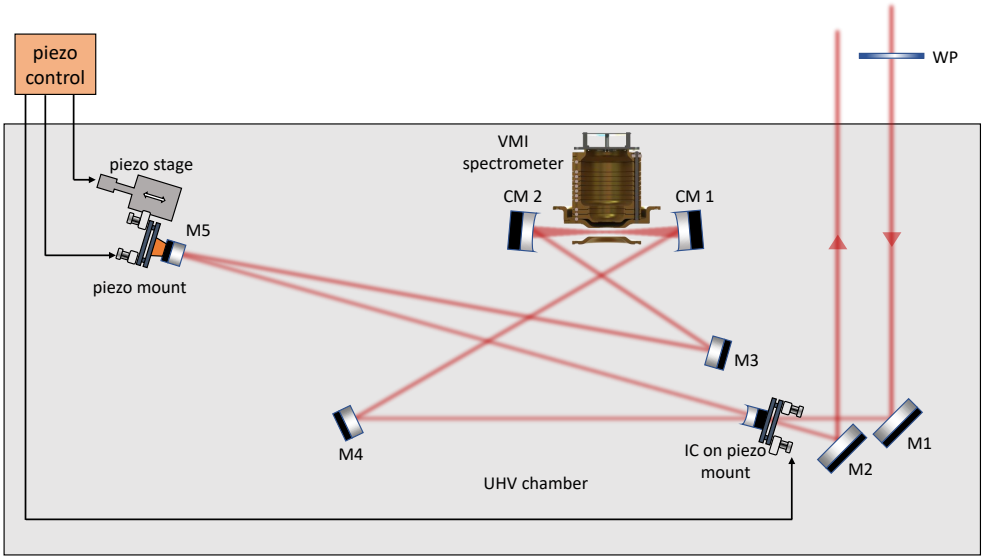

Figure 3.4: Schematic overview of the fsEC. The pulse passes first through a rotatable wave plate for polarization adjustment. The cavity consists of the plane mirrors M3, M4, and M5, the curved mirrors CM1 and CM2, and the input coupler (IC), consisting of a curved mirror with finite transmittance mounted on a piezo mount. The light enters the cavity through IC and is focused between CM1 and CM2, where the VMI spectrometer is located. The laser power can be measured via an intra-cavity power monitor (leakage of M4). The optical length of the cavity is adjusted with M5, which is placed on a piezo mount connected to a piezo stage.

the cavity power as a function of time. Due to the scanning over the resonance, the power is mostly zero except for a short period when the resonance is hit, and the peak power is achieved. In the second method, the cavity is locked on resonance. The resulting power spectrum is shown in Fig. 3.5 (b). The power is mostly stable at the peak power with small fluctuations due to vibrations and imperfect lock electronics. Occasionally the cavity drops out of the lock, visible by the drops in cavity power. The second method is preferable as it can provide a constant power. Unfortunately, the locking mechanism failed during high power operation in our experiment, and the scan method had to be used.

In every measurement, the VMI image is recorded for 90 different angles of laser polarization, which were adjusted using the wave plate in front of the cavity. This method allowed for rotating the distribution around the x axis of the detector. Therefore, recorded images at different angles of the distribution enable tomographic reconstruction.

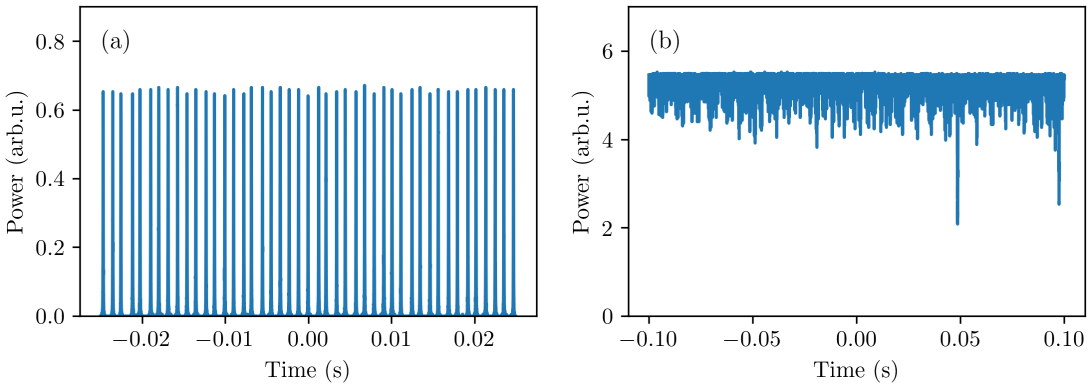

Figure 3.5: Comparison of scan and lock mode for the VMI cavity. (a) The cavity length is oscillated scanning over the resonance. (b) The cavity length is continuously adjusted to lock the power at one power level.

Chapter 4

Pulse Characterization with FROG

Characterizing a laser pulse using raw data with FROG can be complicated for several reasons. First, the iterative retrieval algorithm does not provide an unambiguous solution, i.e., every retrieval yields a slightly different result. An unambiguous solution could only be expected if the measured trace is perfect and relatively simple, i.e., for a pulse shape with low complexity and with negligible noise in the trace. Although some algorithms are considered noise resistant (e.g., ePIE algorithm [39]), noise is still a significant concern regarding stability and repeatability in our retrieval. Moreover, the FROG trace should be physically valid. This means that the SHG FROG trace, in particular, is symmetrical with respect to the zero-delay axis. Therefore, the symmetry of the trace must be achieved before the retrieval procedure. A physically not valid trace can not be reliably retrieved using FROG because the retrieval confirms the measured data's validity and will converge to the closest physically valid trace [48]. This may not be the correct trace in the presence of systematic noise. The retrieval algorithm used in this thesis was implemented by Sven Kleinert in [49].

For the following two chapters, the FROG and iFROG data measured in [22] is used. Both setups were used to perform several measurements with different amplifier settings. However, this work focuses on the measurement at maximal amplification of the frequency comb since this is the generally used setup.

4.1 Measurements

The measured trace can be seen in Fig. 4.1 (a) with the intensity in logarithmic scale. A delay step of 3.33 fs and a wavelength step of 0.012 nm are used. As the first approximation, the autocorrelation of the trace is calculated by integrating over the spectra. The resulting intensity as a function of the delay time is shown in Fig. 4.2. The main pulse has a Gaussian-like shape, with several satellite pulses. However, it is to note, that in both figures, Fig. 4.1 and Fig. 4.2, the trace is not symmetrical with respect to the time delay, in contrast to what would be expected for a SHG FROG trace. The autocorrelation yields only minimal information on the pulse. Therefore, FROG is applied.

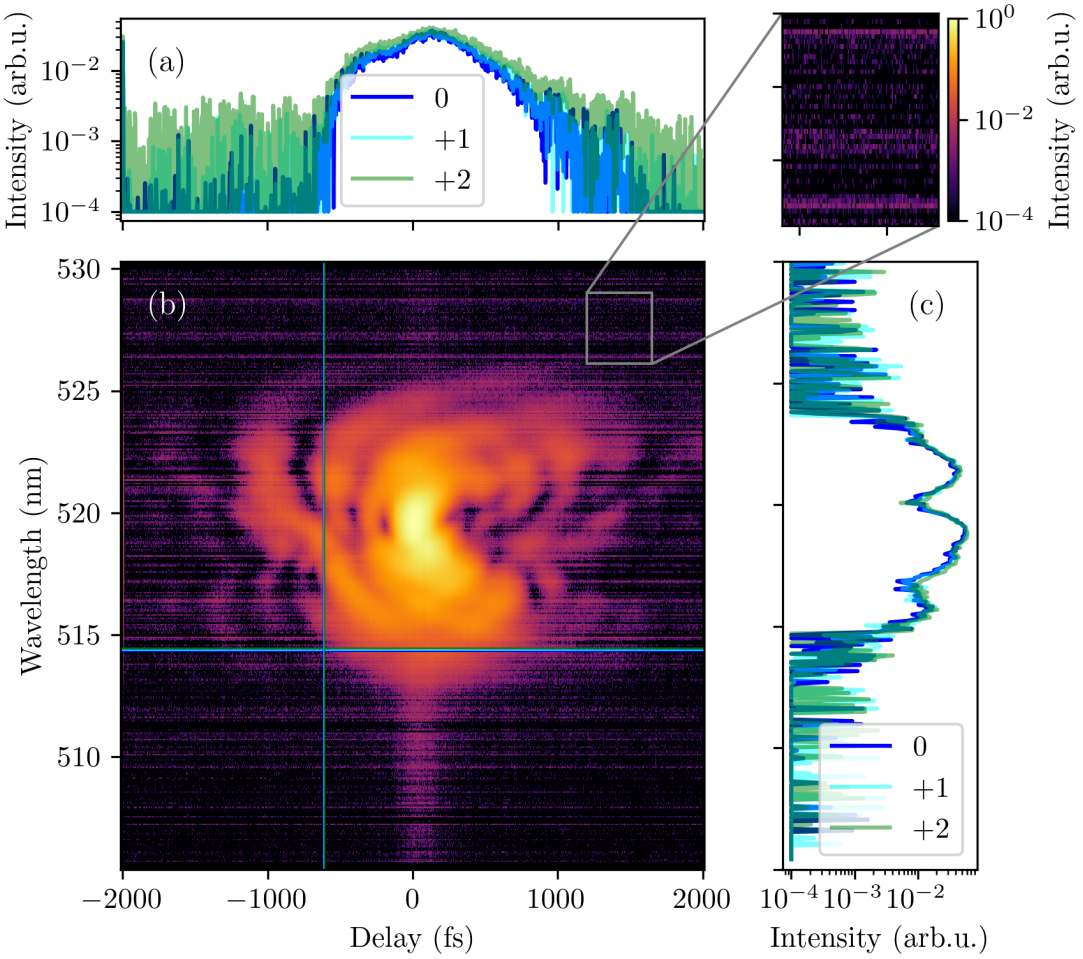

Figure 4.1: (a) and (c) show the slices marked in blue, cyan, and green on the raw FROG trace plotted in (b). The trace, as well as the slices, are shown in logarithmic scale. The inset shows a zoom of the noise.

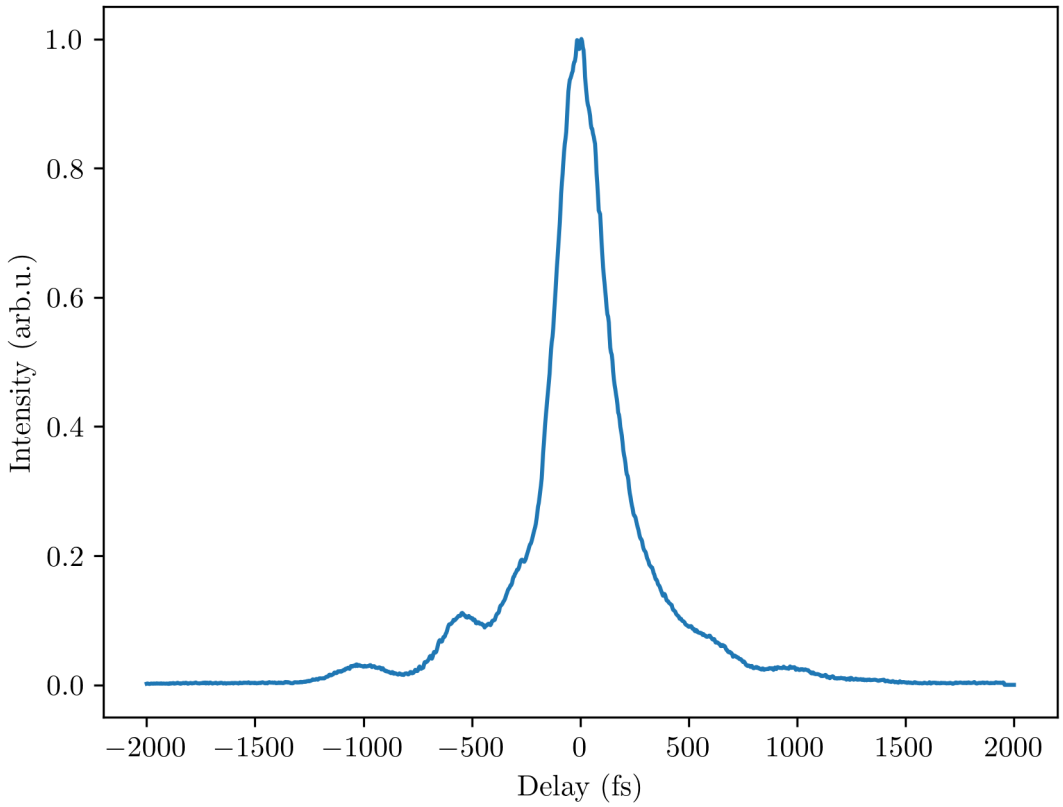

Figure 4.2: Autocorrelation trace corresponding to Fig. 4.1 (a), gained by integrating over the ordinate. The main pulse accompanied by one or several satellite pulses is visible.

4.2 Symmetry Correction

Fig. 4.3 demonstrates the influence of symmetry on the reliability of the FROG retrieval. Fig. 4.3 (a) shows the original trace and Fig. 4.3 (b) the trace, which results from the retrieval with the ePIE algorithm. As mentioned above, the iterative retrieval of a FROG trace yields different results for each run. Therefore, the retrieval is performed several times for every step of the noise cleaning, and the best result is chosen. The quality of the result is assessed using the FROG error, defined in Eq. 2.33, and the similarity between retrieval and original trace. Reproducibility defines an additional criterion for the quality of a trace. Traces resembling valid physical results will have minor fluctuations from retrieval to retrieval since the algorithm has fewer possibilities to minimize the FROG error. Based on the comparison of the measured and retrieved FROG traces, it is concluded that symmetrization is necessary for reliable pulse characterization. A "simple flip" symmetrization function was implemented to improve the retrieval, which first centers the trace and then takes the mean over every two corresponding pixels of the trace

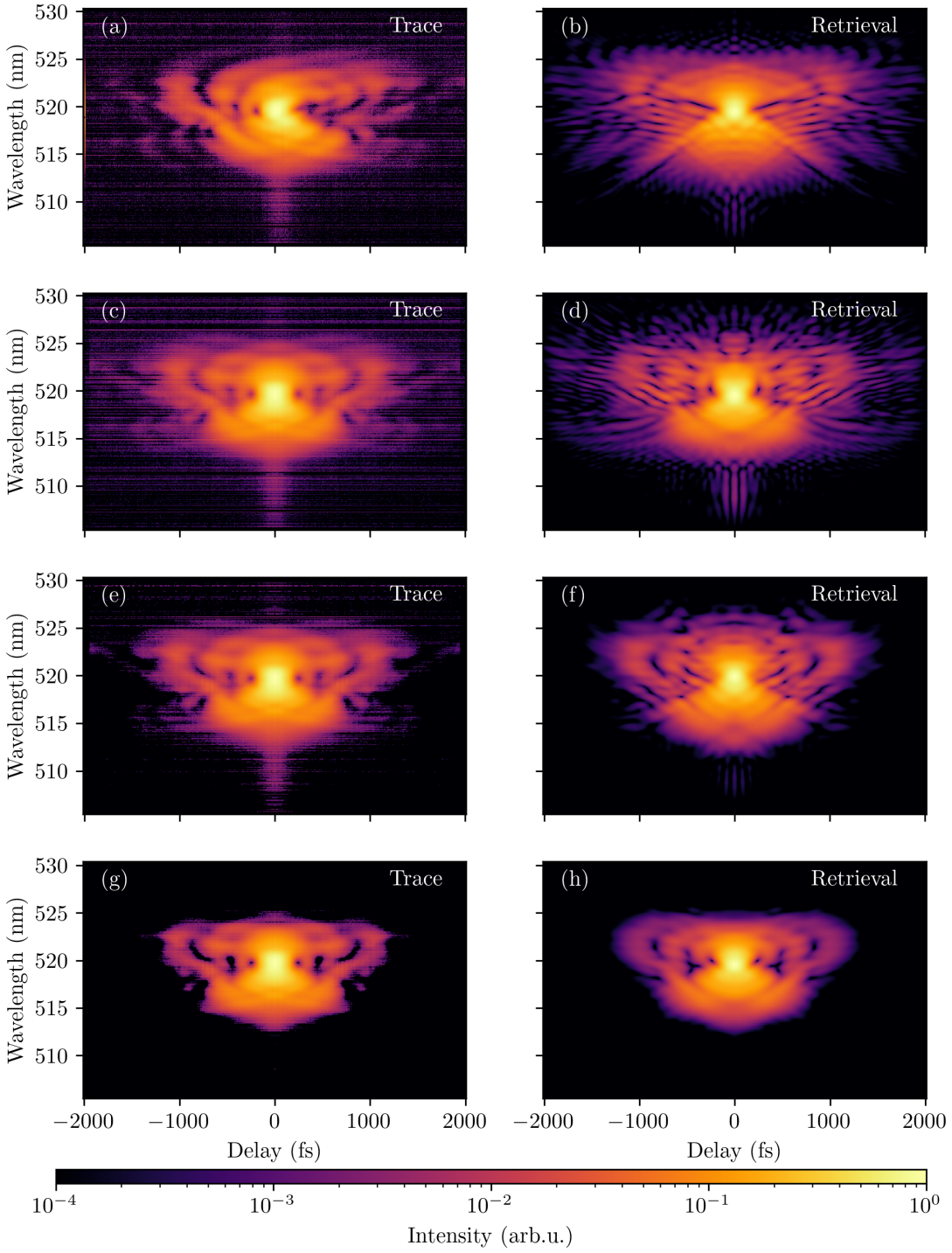

Figure 4.3: Comparison of retrievals for traces with different levels of noise reduction. (Left) shows the original traces. (Right) demonstrates the retrieval traces generated from the electric field retrieved by the ePIE algorithm. (a) shows the raw data. In (c), the "simple flip" method was applied for the symmetrization of the trace. In (e), every noise reduction function was used except for the "lowest pixel" method. In (g), a complete noise reduction was employed. The corresponding retrievals are shown respectively in (b), (d), (f), and (h).

and the along zero-delay flipped version to get a perfectly symmetrical trace. Although this is a simple and rough symmetrization method, additional tests showed that only slight symmetrization using more complex algorithms does not yield a satisfying result. The result of the symmetrization can be seen in Fig. 4.3 (c). This halved the FROG error to $1.51 \cdot 10^{-3}$. For comparison, the trace was also symmetrized by taking only the left or right side and concatenating it with the flipped version, shown in Fig. 4.4 (a) for the left and Fig. 4.4 (b) for the right side.

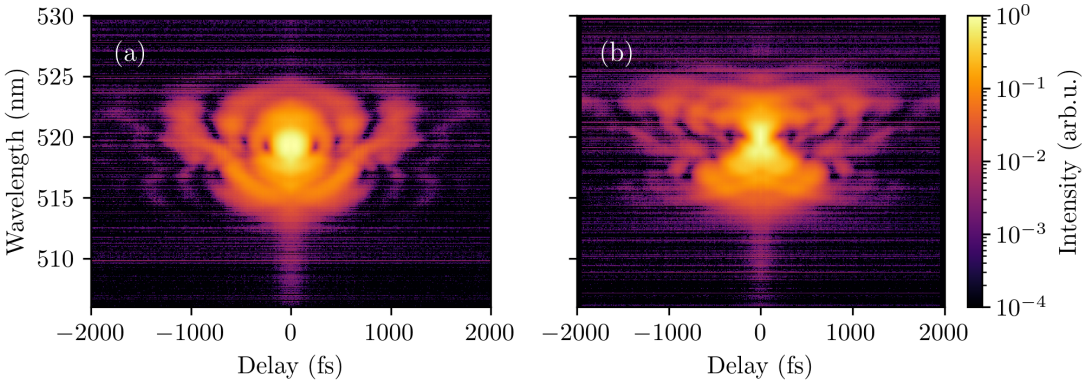

Figure 4.4: Symmetrization of the trace by taking only half of the trace. (a) Trace resulting from the symmetrization of only the left (a) / right (b) half of the original trace.

The retrieval of these traces is significantly worse than for the whole trace, even with noise reduction. Thus, the symmetrization using the "simple flip" method is further used. However, the retrieval does not resemble the original trace sufficiently, even with perfect symmetrization.

4.3 Noise Reduction by Targeted Noise-Removal Algorithms

Several algorithms for denoising the FROG trace are implemented to optimize the FROG retrieval and will be reported in this section. They address two types of noise that can be identified in the trace: (i) Horizontal lines of low intensity, which vary for different measurements, and (ii) the structure above and below the main trace centered at zero-delay. The horizontal lines are visualized in Fig. 4.1 (b) and Fig. 4.1 (c). The blue, green, and cyan-marked adjacent slices are shown in the corresponding colors in Fig. 4.1 (b) and (c), with the intensity in logarithmic scale. A strong noise fluctuation between adjacent horizontal slices is visible, while the noise is constant for vertical slices. The lines are

likely caused by a camera fault and are spread across all delays but fluctuate enough in their intensity and position so that they can not be easily cut out. The structures at zero-delay can be associated with stray light in the spectrometer at high intensities. The following correction algorithms can be performed to reduce the noise:

1. "Edge pixel": The mean value of the two outermost columns to the left and right of the trace is subtracted from the complete trace. The mean is taken along the delay and spectral axis. It is based on the idea that light is not observed at the edge of the trace, and thus, the pixels should all be zero. Thus, any signal registered by the camera is noise and can be subtracted from the trace.

2. "Full spectrum": The mean value of the k outermost columns to the left and right of the trace is subtracted, but the mean is only taken along the delay axis. Thus, noise caused by spectrally dependent but delay-independent stray light is removed.

3. "Pixel cleanup":A Gaussian filter is used to set every pixel with less than k non-zero neighbors to zero. This approach assumes that there should not be any stray pixels with less than a certain amount of non-zero neighbors. This function helps to remove single noisy pixel that may be hard to remove using other functions due to the possible high intensity.

4. "Lowest pixel": The k smallest pixel along a given axis are subtracted to remove any noise which could not be eliminated with the previous algorithms.

After every denoising procedure, negative values are set to zero, as negative intensities should not occur in a FROG trace. The following noise reduction algorithms were sequentially used for the trace shown in Fig. 4.3 (g):

1. Pixel cleanup
2. Edge pixel
3. Lowest pixel (k = 50, axis = 0)
4. Full spectrum (k = 50)
5. Center trace
6. Correct symmetry

7. 3 x Pixel cleanup (k = 4)

These noise reduction steps are the most suitable for reducing the FROG error. The retrieval shown in Fig. 4.3 (h) resembles the original trace, and the structures inside the trace are visible in the retrieval. The error for this retrieval is $1.41 \cdot 10^{-3}$, with fluctuations between $2.0 \cdot 10^{-3}$ and $1.0 \cdot 10^{-3}$. The axis of the "lowest pixel" function was chosen as 0 because the noise lines are horizontal.

Non-selective removal of noise in the "lowest pixel" procedure inevitably leads to the elimination of some parts of the trace. Therefore, the same noise reduction steps, except for "lowest pixel", are used to evaluate the need for the "lowest pixel" denoising. The result is shown in Fig. 4.3 (e). The corresponding retrieval displayed in Fig. 4.3 (f) demonstrates that complete removal of noise is essential because otherwise, the algorithm interprets the noise as part of the signal. Although the FROG error is not significantly higher than before ($1.51 \cdot 10^{-3}$), comparison with Fig. 4.3 (h) shows that the resemblance between retrieval and original trace becomes better if the noise is completely removed. An observation regarding the FROG error is: a smaller FROG error does not automatically mean an improvement of the retrieval since overfitting might lead to the minimization of the error while the retrieval is deviating from the original trace.

The results of the pulse characterization for the above-described noise reduction steps are shown in Fig. 4.5. The figure labels correspond to the same level of noise reduction as in Fig. 4.3. On the left, the power spectral density (PSD) is shown in blue and the spectral phase in brown. The spectral phase is only defined in the range of the PSD and is expected to be constant since our pulse should not have any chirp. This is mostly true for the retrievals. On the right, the pulse's intensity and temporal phase are shown as a function of time by blue and brown lines, respectively. At least one satellite pulse is present in all retrievals, which was also visible in the autocorrelation. The retrieved shape and width of the main pulse vary strongly between the different levels of noise removal. The first two cases, without noise reduction, do not demonstrate the expected Gaussian shape but have an artifact at the top of the curve. Moreover, the pulse duration varies strongly between 160 fs and 210 fs in every run. The last two cases have a retrieved pulse width of ∼180 fs, but only the last one shows the expected Gaussian shape. Besides, the stability of the retrieval is better for the last configuration. In SHG FROG, positive and negative time values are not unambiguously defined. Therefore the position of the satellite pulse to the left or right side of the main pulse is equivalent.

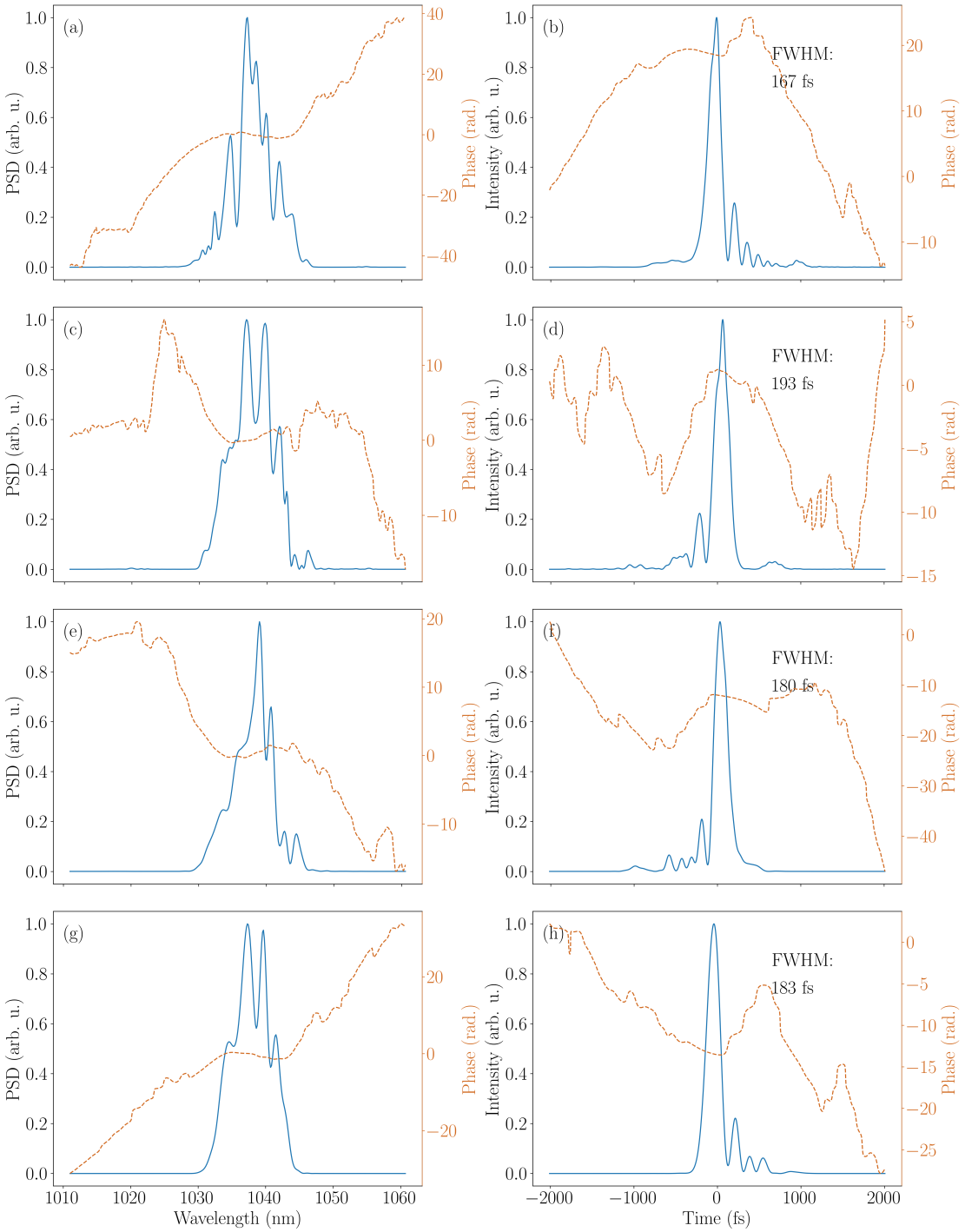

Figure 4.5: Comparison of the retrieved pulses for different noise-cleaning steps as shown in Figure 4.3. (Left) retrieved power spectral density (blue curve) and spectral phase (brown curve). (Right) intensity of the pulse as a function of time (blue curve) and temporal phase (brown curve).

The retrieved PSD from Fig. 4.5 (g) is compared with the separately measured spectrum in Fig. 4.6.

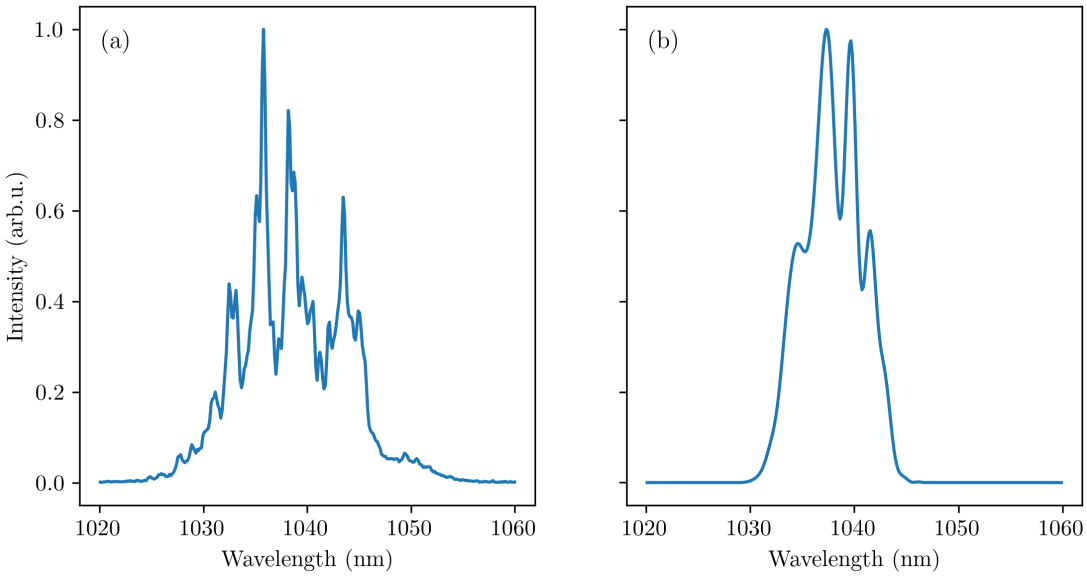

Figure 4.6: Comparison of the separately measured spectrum (a) and the with FROG retrieved spectrum (b).

The spectrum is not accurately retrieved since several large and small structures are missing. It has to be taken into account that the comb-like structure underlying the envelope is not resolved in Fig. 4.6 (a) because of the limited resolution of the spectrometer. It is likely that the noise reduction algorithms remove some structures of the trace and thus oversimplify the retrieved spectrum. By comparison with Fig. 4.5 (a) it is visible that more spectrum details are retained without noise reduction, although it is still far from the original spectrum. Since the PSD is generated by a Fourier transform from the same retrieval as the temporal pulse shape, structural details are also likely missing in the temporal pulse representation. Fig. 4.5 (c) demonstrates that solely the symmetrization procedure already significantly decreases the resolution of the resulting spectrum. Therefore, it must be admitted that the temporal and spectral retrieval accuracy is strongly limited by the quality of the present experimental data. Due to the instability of the retrieval, large FROG error, and dissimilarity of trace and retrieval, denoising procedures, especially symmetrization, are essential to achieve a good retrieval of the temporal pulse shape. Since the spectral shape of the pulse can be measured directly, the retrieval will be further assessed by the quality of the temporal pulse shape. From this point of view, the noise reduction protocol used in Fig. 4.3 (g) yields superior results

compared to other protocols. Lack of symmetry and systematic noise in the trace pose significant problems for retrieval. It may be that Gaussian noise applied to the whole trace may have a negligible effect on the retrieval. However, since the present noise has the distinct shape of horizontal lines, the algorithm tries to include them in the retrieval and thus yields inaccurate results despite a small FROG-error.

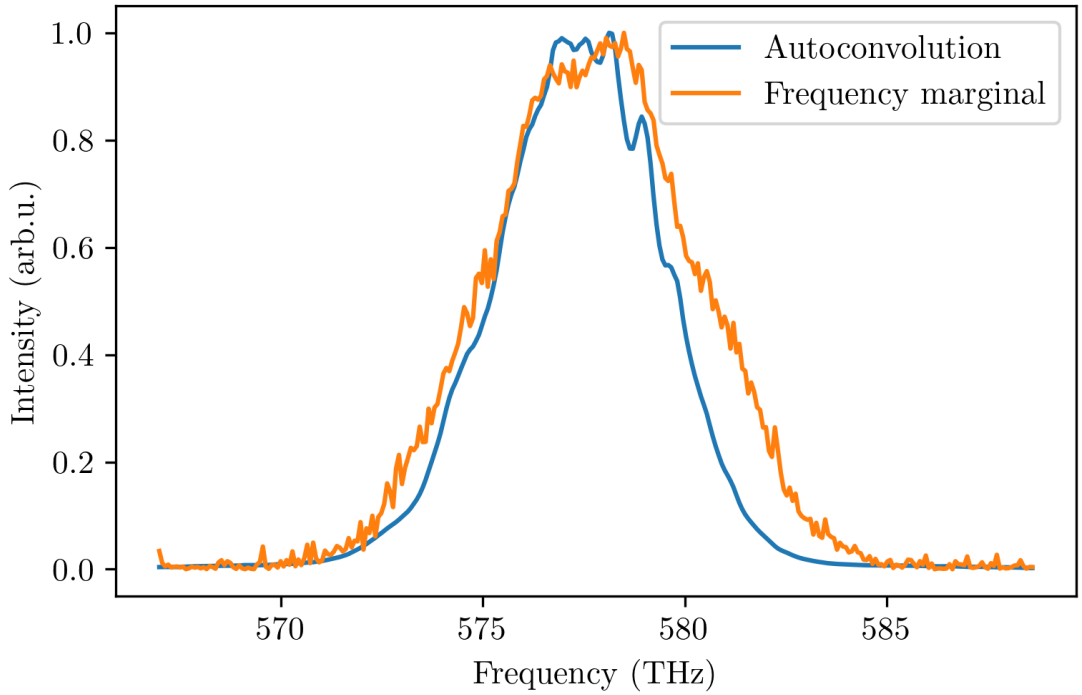

Figure 4.7: Comparison of the frequency marginal of the FROG trace (orange) and the autoconvolution of the measured spectrum (blue).

To evaluate the quality of the measured data from a different perspective, the frequency marginal $M(\omega)$ of the FROG trace defined as

$$M(\omega) = \int I_{\mathrm{FROG}}(\omega, \tau) d\tau, \tag{4.1}$$

is compared with the autoconvolution $M_{\mathrm{SHG}}(\omega - 2\omega_0)$ of the measured spectrum $I(\omega - \omega_0)$

$$M_{\mathrm{SHG}}(\omega - 2\omega_0) = I(\omega - \omega_0)^* I(\omega - \omega_0). \tag{4.2}$$

The frequency marginal should be equal to the autoconvolution of the spectrum [50]. However, as shown in Fig. 4.7, while for low frequencies, the difference between the frequency marginal and autoconvolution is small, for high frequencies, the intensity of the frequency marginal is notably higher than the autoconvolution. Further, well-

resolved peaks observed in the autoconvolution are missing in the marginal. As shown exemplarily in [50] differences between the marginal and the autoconvolution yield a wrong spectrum retrieval and indicate a systematic error in the measurement.

4.4 Noise Reduction by Background-Subtraction

The targeted noise reduction discussed above is extremely easy to fine-tune due to the variety of employed functions and parameters. However, the "lowest pixel" function, which ensures the complete removal of noise in the FROG trace, also removes some relevant parts of the trace together with the noise. It is therefore unclear whether targeted noise reduction can ensure a higher accuracy than more general and less selective approaches. Thus, two generic approaches are additionally tested, and the results are compared with those obtained from the targeted noise reduction. As shown in Fig. 4.1, the noise fluctuates strongly between horizontal slices. Therefore, the spectral resolution is reduced by averaging over several adjacent horizontal slices, allowing to subtract the noise as a constant background. The result for the case of five-line averaging is illustrated in Fig. 4.8. Fig. 4.8 (a) shows three adjacent horizontal slices of the raw trace, while Fig. 4.8 (b) depicts the slices of the trace with a reduced spectral resolution. The improvement in signal-to-noise ratio is visible.

Another approach to smoothing the image that could be applied is the Savitzky-Golay filter, proposed in 1964 by Abraham Savitzky and Marcel J. E. Golay [51] as a method to pre-process noisy images. The filter uses the linear least-squares method in connection with convolution to fit a polynomial function to sections of the trace, thus reducing the noise while preserving the main structures. This method is in most cases superior to the simple averaging done before, as shown exemplarily in [52], but in our case, the horizontal lines are a significant structure in the image included in the least-squares fit. Tests showed that the least-squares fit has to be applied to large areas to generate an equally good signal-to-noise ratio as with the mean.

Finally, the background noise can be removed from the trace using a simple intensity cutoff. Specifically, every pixel with an intensity lower than the cutoff value is set to zero. The result with a cutoff intensity of 0.004 is plotted in Fig. 4.9 (a).

The cleaned image is remarkably similar to the noise cleaning result using the targeted noise reduction. The retrieved trace, shown in Fig. 4.9 (b), and pulse are also

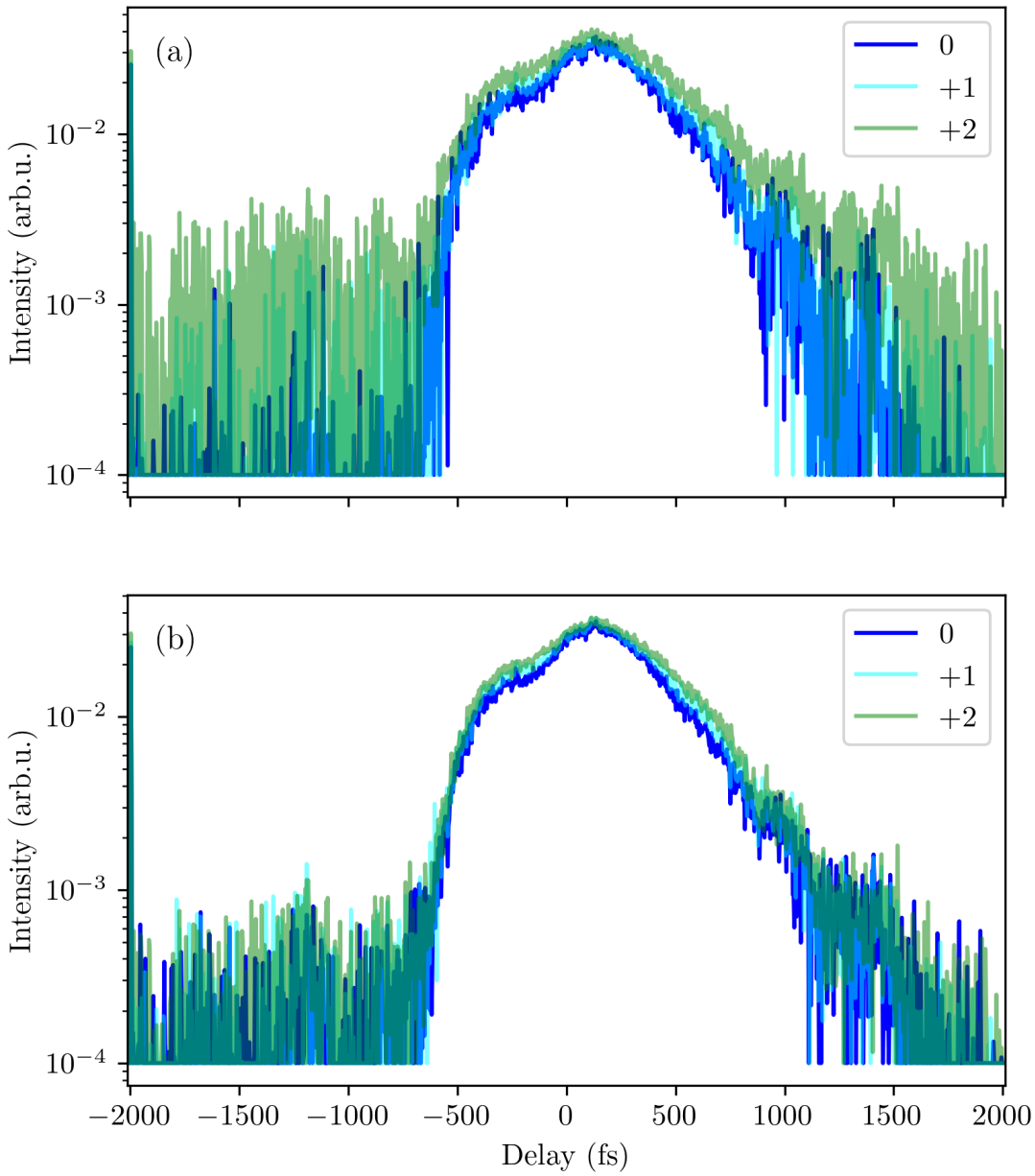

Figure 4.8: Three adjacent horizontal slices are shown in (a) for the raw trace as in Fig. 4.1 (a) with the same color-coding. (b) shows the same slices for a trace with reduced spectral resolution. A significant improvement in the signal-to-noise ratio is visible in (b).

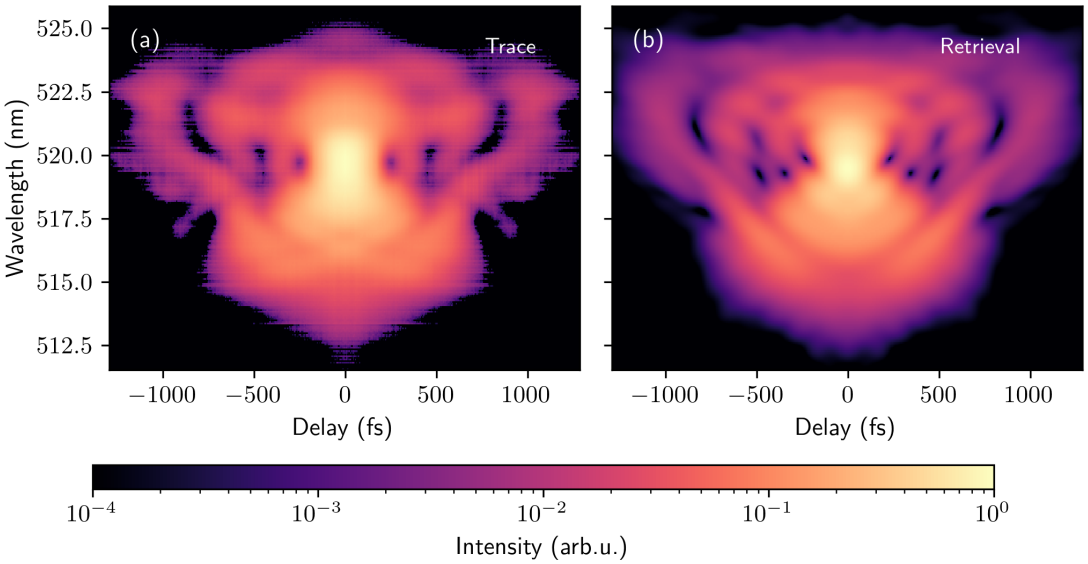

Figure 4.9: (a) Trace after noise reduction through averaging over spectral slices and then setting every pixel with a lower intensity than 0.004 to zero. (b) shows the retrieval of (a).

nearly identical. Thus, the same results are achieved with background subtraction and targeted noise reduction. Due to the possibility of fine-tuning, the targeted noise reduction is preferable to the background subtraction.

4.5 Retrieval

Further retrieval improvement is tried by adding additional noise when the ePIE algorithm starts stagnating. This procedure significantly reduces the FROG error but does not improve the quality of the retrieved trace due to overfitting. This result demonstrates the trend mentioned above that an error reduction often means that the ePIE algorithm overfits the trace and thus leads to an unreliable retrieval.

4.6 Pulse Characterization

Based on the analysis reported in the previous Sections, the pulse FWHM is determined as 183 fs. The error yielded by observation of the fluctuations across different retrievals of the same trace is ∼3 fs. Unfortunately, the systematic error of the symmetrization, noise reduction, and experimental errors can not be reliably estimated and therefore is not included in the uncertainty. The comparison of the measured spectrum and retrieved

PSD suggests that the noise reduction and symmetrization algorithms simplify the trace and, thereby, the retrieved temporal and spectral pulse shape. The similarity between the temporal retrieval with noise removal using targeted noise reduction and background subtraction suggests that the simplification affects the spectral domain predominantly. Due to an easier pulse alignment and since it also allows the usage of the delay stage for additional experiments without changing the setup, the pulse characterization was repeated in the following chapter using iFROG.

Chapter 5

Pulse Characterization with Interferometric FROG

The general method for pulse characterization with iFROG is described in Chapter 2. The method's main idea is to use a low pass filter on the iFROG trace to get the intensity FROG trace with a constant background, which can be subtracted from the trace. The resulting trace can then be retrieved using ePIE.

5.1 Preprocessing

The measured iFROG trace is shown in Fig. 5.1 (b). The delay step is reduced to 0.2 fs to record the interferometric fringes visible in the plot. Therefore, more points are measured so that the whole trace is recorded. The wavelength step is the same as in the intensity FROG measurement since the same spectrometer was used. As for FROG, the autocorrelation can be calculated for iFROG in the same way by integrating over each spectrum. The resulting intensity is plotted in Fig. 5.1 (a) as a function of the delay. The low resolution of the plot does not allow for distinguishing every interferometric fringe. Therefore, only the modulation curve is visible. The second harmonic background resulting from both separate pulses can be identified as the intensity offset. The trace is not symmetric regarding zero-delay and thus does not fulfill the SHG requirement. The image in Fig. 5.1 (d) is generated by Fourier transformation of the delay axis. Five Fourier components are visible in the logarithmic plot and in the horizontal slice at the central wavelength in Fig. 5.1 (c). A low pass filter is applied to the trace with a cutoff frequency of 0.012. The resulting trace and autocorrelation, presented in Fig. 5.2, are

very similar to the theoretical result shown in Chapter 2.

The background is visible in the trace as spectrally dependent but constant along the delay. The autocorrelation has no longer interferometric oscillations but still retains an offset from zero due to the constant background. Therefore, the "full spectrum" noise reduction function with $k = 10$ is applied to the trace, which yields a background-free trace. For visualization and better retrieval, the delay is sampled down to be closer to the delay of the FROG trace by interpolating between the existing values. The resulting trace and its autocorrelation are shown in Fig. 5.3 (b) and Fig. 5.3 (c) (orange curve), respectively, and compared to the autocorrelation of the measured FROG trace and the trace itself shown in Fig. 5.3 (c) (blue curve) and Fig. 5.3 (a).

This visualization clearly shows that the iFROG trace is not complete. Specifically, the measurement captured only the central part of the trace, cutting off part of the satellite pulse. The central peak and the peak of the satellite pulse remain at the same positions.

5.2 Pulse Characterization

The extracted FROG trace is retrieved using the ePIE algorithm. As discussed in the previous Chapter, the retrieval strongly depends on the pre-processing quality. A closer view of the noise behavior is shown in Fig. 5.3 to consider this in detail, where the measured FROG trace and the processed iFROG trace are shown in logarithmic scale. The horizontal lines from the FROG trace are missing in Fig. 5.3 (b), but the noise around the center of the delay axis is visible. Moreover, the trace is not symmetrical. Therefore, the "simple flip" algorithm is used first to symmetrize the trace. Since no horizontal lines are visible, the noise can be directly removed as the background of the trace. The optimal threshold for the background intensity was found to be 0.006. The result is shown in Fig. 5.4. Specifically, the trace after noise cleaning and the retrieved trace are illustrated in logarithmic scale in Fig. 5.4 (a) and Fig. 5.4 (b), respectively. Fig. 5.4 (c) and (d) show the pulse shape in blue and phase in brown for the temporal and spectral domain, respectively.

The resulting FROG error is $1.75 \cdot 10^{-3}$. The whole noise is removed, which caused cutting out some trace structures. As has been shown for the FROG retrieval, it is better to completely denoise the trace, even at the expense of the loss of some part of

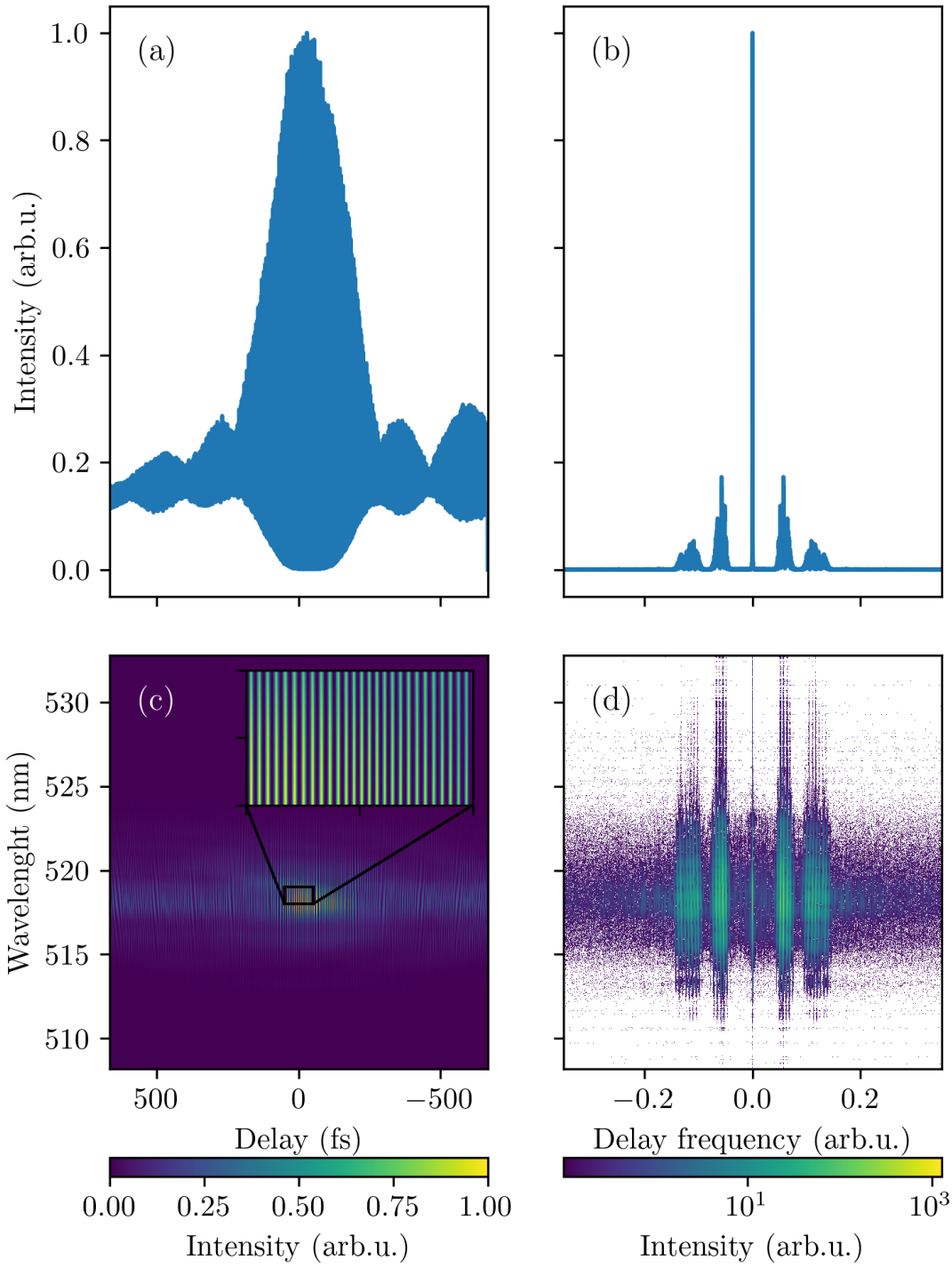

Figure 5.1: Fourier analysis of the measured raw iFROG trace in the same way as in Fig. 2.8. (a) shows the autocorrelation of the iFROG trace shown in (c). (d) presents the Fourier components of (a), with the horizontal central slice at 520 nm in (b).

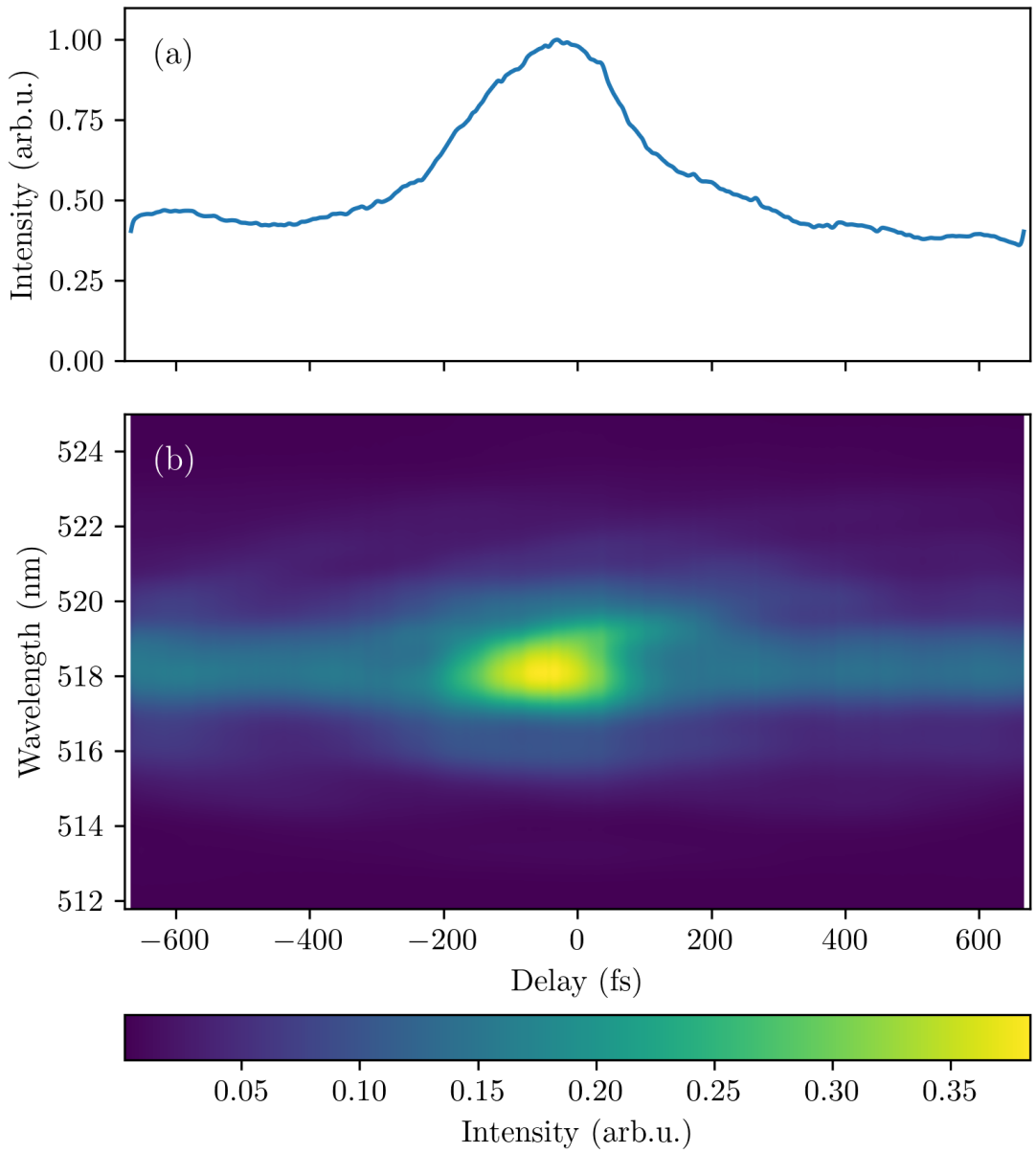

Figure 5.2: (a) shows the autocorrelation of the trace in (b). The trace is the low pass filtered iFROG trace from Fig. 5.1 (c). In (a) and (b) the interference fringes visible in Fig. 5.1 (a) and (c) are missing. The delay independent background is visible in (a) as an offset from zero.

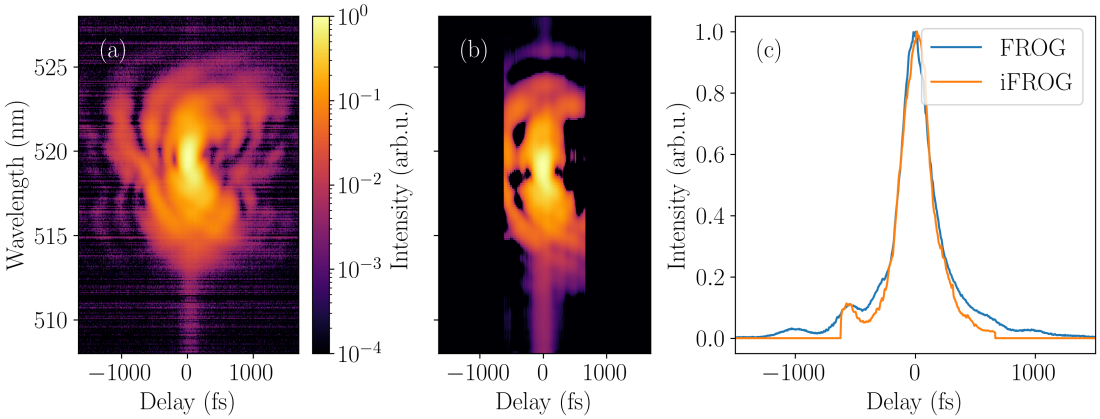

Figure 5.3: (a) shows the measured FROG trace. (b) shows the FROG trace generated from Fig.5.1 (c) using a low pass filter, background subtraction and downsampling. (c) Autocorrelation of (a) in blue and (b) in orange. The delay step in (a) is 3.3 fs and in (b) 2 fs. The traces are plotted in logarithmic scale.

the pulse structure. The retrieval resembles the original trace, and the retrieved pulse shows only a slightly tilted Gaussian form. Since the spectral phase is not constant, it is retrieved worse than with FROG. The PSD does not resemble the separately measured spectrum. The additional peaks in the temporal dimension look distorted compared to the FROG retrieval in the previous chapter. The FWHM is retrieved as 178 fs but fluctuates strongly between retrievals.

The result of the iFROG pulse characterization demonstrates that this is an appropriate method for this experiment. The result is similar to FROG, although only a partial trace was measured. Further investigation is required to evaluate the possibility of achieving a retrieval quality in iFROG comparable to that of FROG.

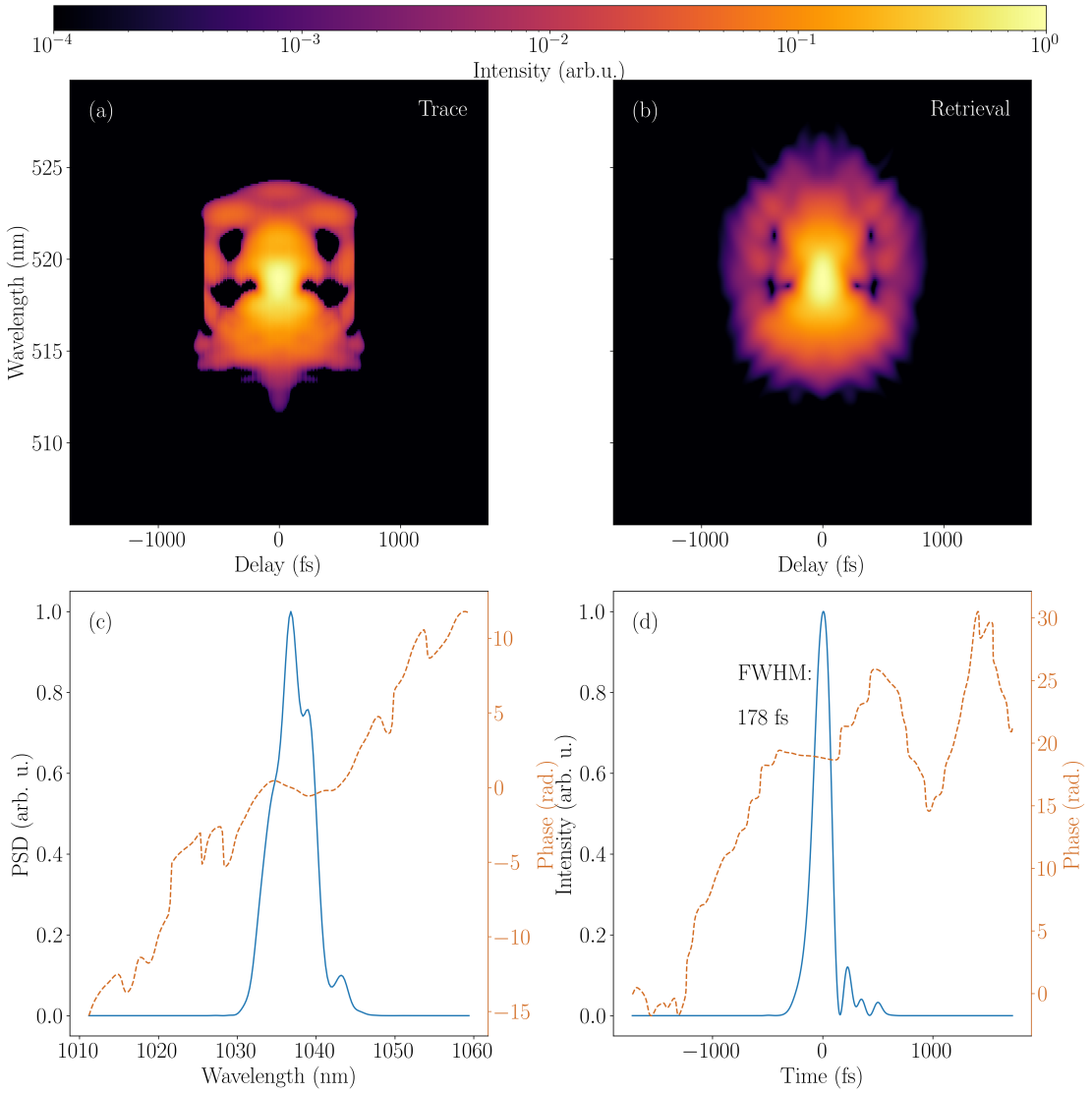

Figure 5.4: Retrieval of iFROG trace after background filtering. (a) Fig. 5.3 (b) after noise cleaning by removing the background. (b) Retrieval of (a) using the ePIE algorithm. (c) Retrieved spectrum and spectral phase. (d) Retrieved pulse and temporal phase.

Chapter 6

Velocity Map Imaging

Based on the above characterization of the laser pulse, the properties of the by VMI measured photoelectron angular distributions (PADs) can be investigated. For this, artifacts caused by the MCP and CCD-camera are removed from all images, and then, the electron energy spectrum is calibrated by retrieving the energy of the first VMI ring. This is compared with the theoretically calculated energy spectrum.

6.1 Measurements

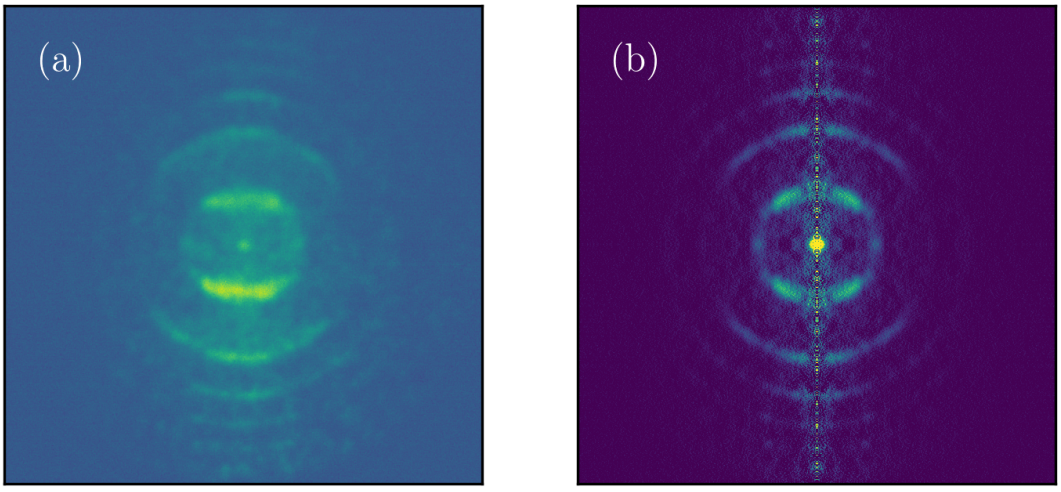

Figure 6.1: Measured VMI image and its Abel transform. (a) Example of a VMI measurement. (b) Result of the inverse Abel transform of (a).

An at p-polarization recorded example of the measured PADs with the characteristic circles of VMI is shown in Fig. 6.1 (a). From this image, a 3D electron distribution is

reconstructed using the inverse Abel transform. A slice through the resulting distribution is shown in Fig. 6.1 (b). Noteworthy, only the edge of the distribution is shown instead of the full projection.

6.2 Artifact Correction

The noise of the images must be reduced as much as possible to reconstruct a 3D electron distribution. Tomographic reconstruction is especially sensitive to noise that remains unchanged throughout all measurements. Artifacts, hot pixels, and defective pixels are the dominant noise sources in the recorded raw images.

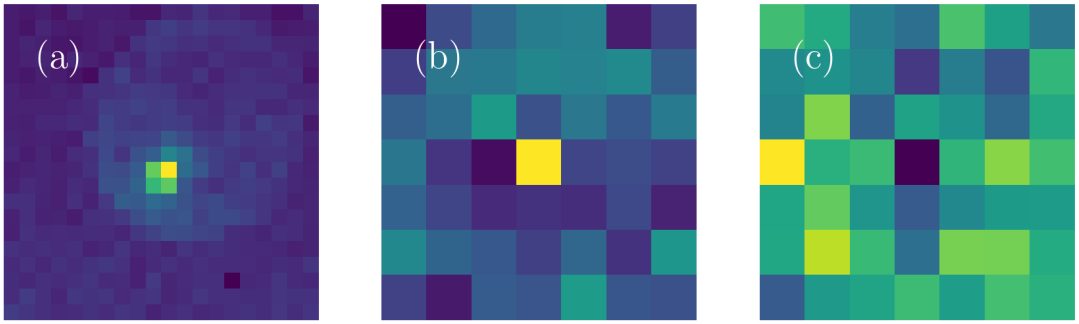

Figure 6.2: Comparison between an exemplary artifact (a), hot pixel (b), and defective pixel (c).

An artifact (see Fig. 6.2 (a)) is the result of an error in the MCP, which leads to a continuous firing of one channel and is thus recorded as a structure of higher intensity extended over several pixels. In this case, the artifact size is approximately 20×20 pixels due to the constant size of the channels. A hot pixel (Fig. 6.2 (b)) is caused by a pixel of the CCD camera that constantly provides a high output, which is visible as a single high-intensity pixel in the image. The reverse phenomenon is a defective pixel (Fig. 6.2 (c)), which causes constantly a zero-intensity output.

The artifact correction process is based on a previous bachelor thesis [53]. Specifically, since all the above-described types of noise are invariant to the PAD, artificial structures that retain their position across all images can be considered noise. As shown in Fig. 6.2 all noise types are characterized by a maximum or minimum of intensity. Thus, a maximum and minimum filter are applied to every image, and the number of maxima in every pixel throughout the images is counted to locate the noisy pixel. This procedure shows, however, that the assumption that the noise exists for every image in

the same position is not always valid. Therefore, a threshold was set for the minimum percentage of images in which the maximum or minimum of intensity must be observed.

Additionally, to account for the slight movement of the maxima, the reduced image was calculated by taking the mean over squares with a specific size and then identifying the maxima in the reduced image. These maxima were centered and added to the list of the other maxima. The centering is vital since the high-intensity pixel could lie anywhere in the square over which the mean is taken, leading possibly to two overlapping artifacts. The latter can lead to the appearance of surfaces with significantly lower intensity during artifact correction.

The identified maxima are then categorized as artifacts or hot pixel, depending on the surrounding intensity. If the intensity at the maximum is larger than the mean of the surrounding, plus a threshold times the standard deviation of the surrounding, then the maximum is categorized as a hot pixel. This is based on the idea that a hot pixel should have a significantly higher intensity than any surrounding pixel. The surrounding consists of the pixel with maximum intensity and all adjacent pixels. The hot pixel and defective pixel are removed by taking the mean over the adjacent pixel and setting the noisy pixel to that value. For the artifacts, a 20×20 circle is defined as the artifact, which is replaced by a least-squares fit of the surrounding pixels.

The artifacts, hot pixel and defective pixel are illustrated in Fig. 6.3 (a), (c) and (e), respectively, before the removal and in Fig. 6.3 (b), (d) and (f) after removal. The hot pixel and defective pixel are typically all detected and corrected. For the artifacts, false positives are possible. Generally, it is preferable for reconstruction to minimize false negatives, while false positives are less important. A wrongly identified artifact reduces the quality of the image, but an artifact that was not found is obvious in tomographic reconstruction. Therefore, the artifacts are printed after every noise-cleaning as shown in Fig. 6.3 and manually evaluated.

6.3 Energy Calibration

The VMI measurement yields an image where the position on the detector is proportional to the initial momentum of the particle. The radius of the ring R can be calculated from

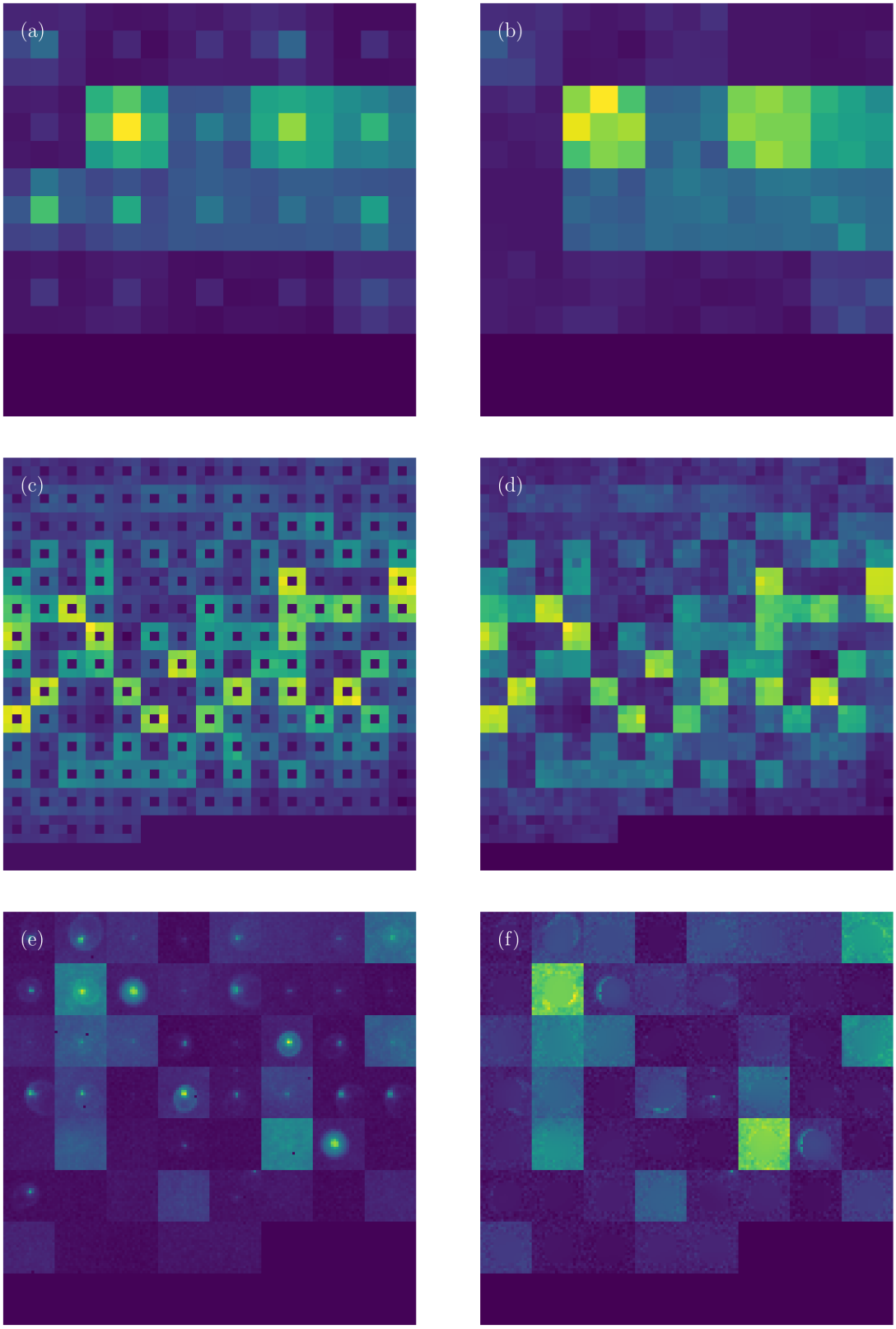

Figure 6.3: Comparison of artifacts (a), hot pixel (c), and defective pixel (e) before removal and after removal in (b), (d), and (f), respectively.

the initial velocity v using an expansion factor N and the time-of-flight t [2]

$$R = Nvt. \tag{6.1}$$

For our experiments, the initial velocity of the particles is unknown; therefore, another method is used to calibrate the detector. The energetic difference between the rings is known to be equal to the energy of one photon. Thus, the radius can be calibrated by fitting the ring centers.

First, the images are inverse Abel transformed and then integrated over the polar coordinates using the PyAbel python package [45] to obtain the ring positions. The resulting image is shown in Fig. 6.4, where the intensity is plotted as a function of the radius. A Gaussian fit is applied to each of the first three maxima. The fit for the fourth maximum yielded a high fluctuation in the results and thus is dropped. The error for the peak position is estimated by the σ value of the fitted Gaussian, as it provides the best representation of the ring width. This procedure is performed for every image at p-polarization from the same dataset recorded in scan mode, which was also used in our previous work to tomographically reconstruct 3D PADs [5]. For other angles, the rings are tilted due to the projection of the 3D distribution, as can be seen in Fig. 6.5.

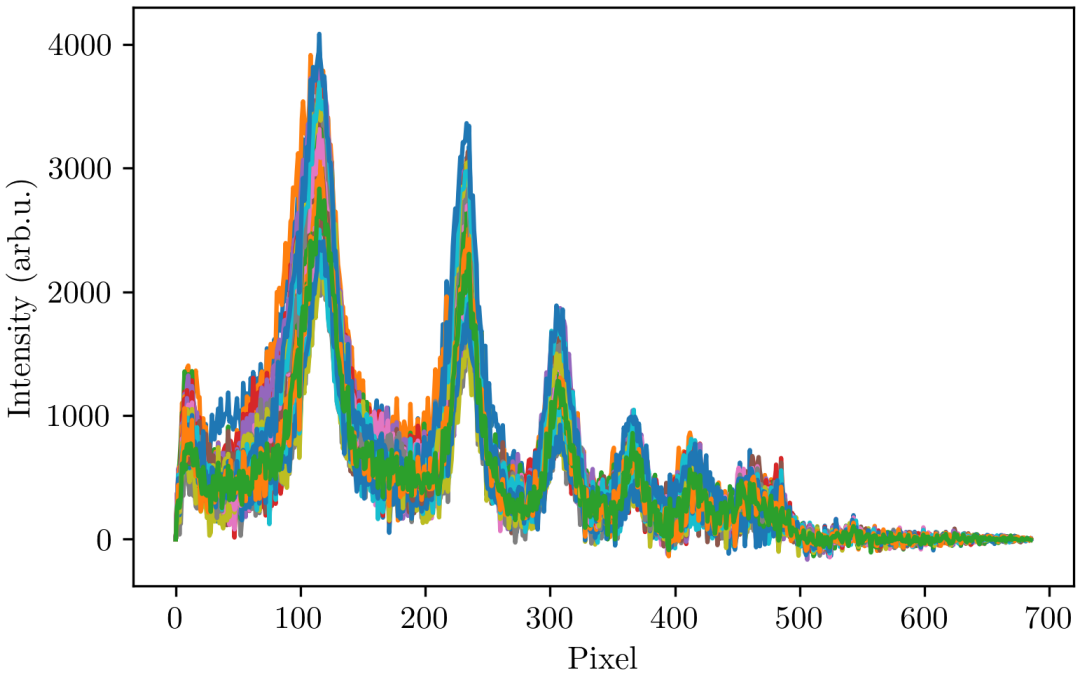

Figure 6.4: Intensity as a function of the radius in a VMI image. Each color corresponds to the photoelectron spectrum obtained by angular integration of a single detector image.

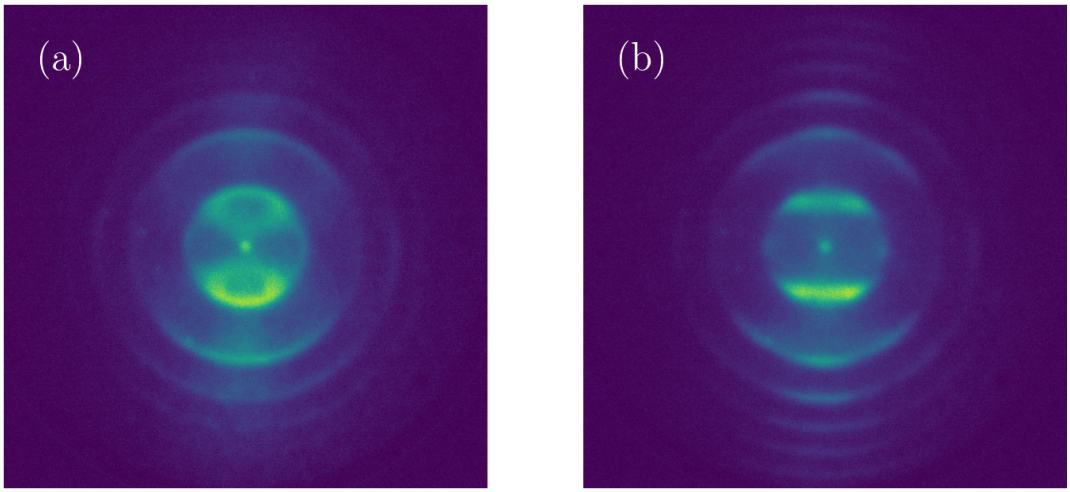

Figure 6.5: VMI image for a polarization angle equal to 73° (a) and 56° (b). At 56° the laser is p-polarized to the detector.

At p-polarization, 33 images are recorded with varying power. Since the ponderomotive shift depends on the laser power, the radius of the rings also depends on the power. Therefore, every image is analyzed separately. The power dependency is illustrated in Fig. 6.6 (a) for the radius and in Fig. 6.6 (b) for the amplitude of the first ring.

Due to the linear dependency of the ponderomotive shift on the laser power, the radius should be proportional to the square root of the power. However, this is hard to identify in the plot, as only a few measurement points with a small power interval are available. The amplitude should depend to the power of 11 on the laser power, which is also not visible in the plot, as the power is changed only by a small amount in the recorded interval.

Since the radius is proportional to the initial momentum, it has a quadratic dependency on the initial energy. Therefore, a quadratic curve with the form of

$$E = a \cdot x^2 - c \tag{6.2}$$

is fitted to the centers of the rings. Here E is the energy of the center. The energy of the first ring is set to zero and the energy difference between the rings is given by $\hbar\omega$. $\hbar$ is the reduced Planck constant, and ω the angular frequency of the photon; a is the calibration factor with which a radius x in units of pixel can be transformed into an energy; c is the energy of the first ring, in units of $\hbar\omega$, equal to $11\hbar\omega - U_p - I_p$. The energy of the photon, $\hbar\omega = 1.19\,\mathrm{eV}$, is used for the fit, shown exemplary in Fig. 6.7 (a) for the highest

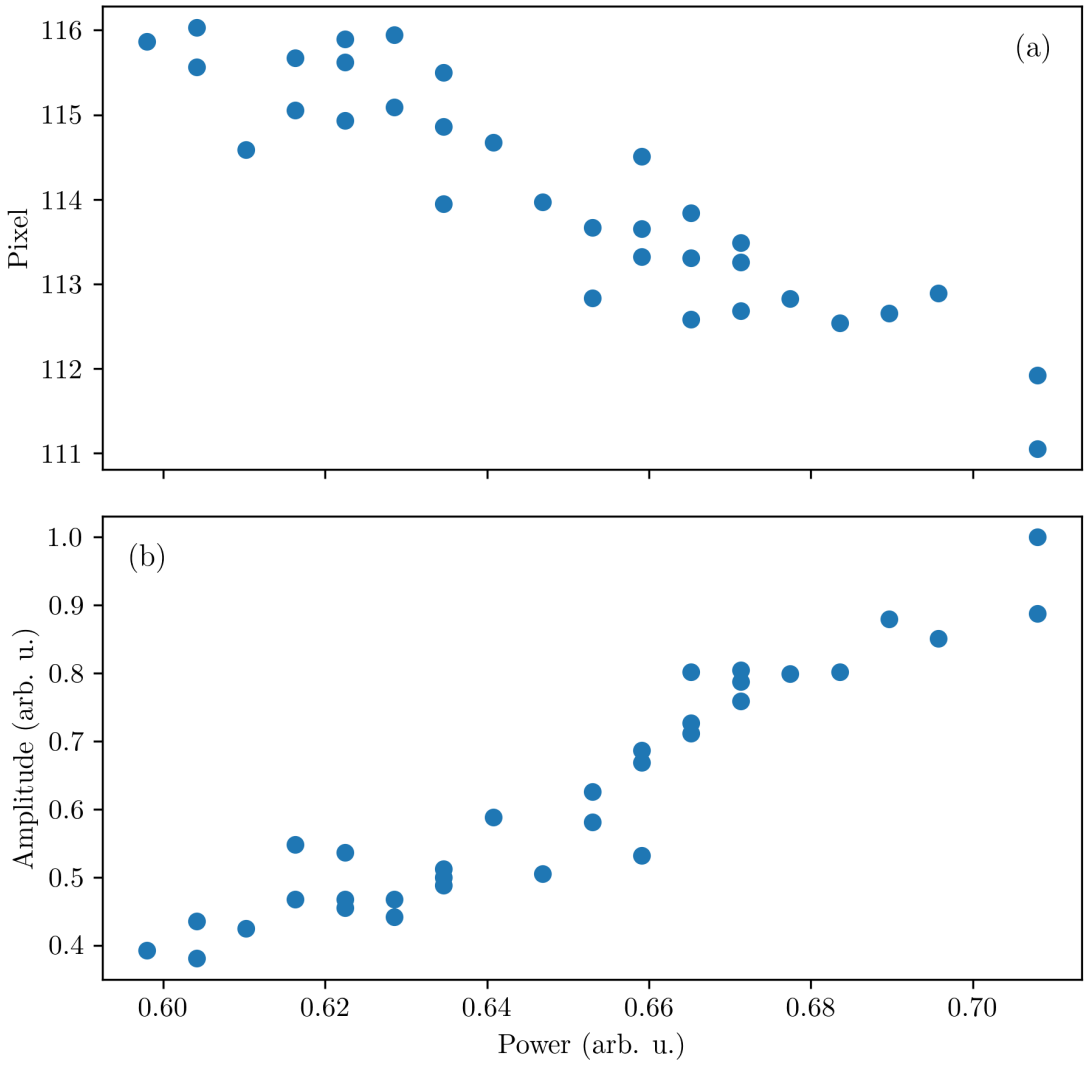

Figure 6.6: Dependency of the VMI image on the power: The center (a) and amplitude (b) of the first ring are shown as a function of the laser power.

and lowest laser power. The factor of the quadratic term is expected to be independent of the laser power, and the difference between the two curves should lie in the offset c. Indeed, this relation is observed in Fig. 6.7 (a) since the green curve for the smaller power is constantly lower than the red curve for the higher power. Fig. 6.7 (b) shows the variation of the energy of the first ring with laser power, which is caused by the change of ponderomotive shift. The final energy calibration was estimated through the mean of the values for each image as $a = (2.9408 \pm 0.0026) \cdot 10^{-5}\,\mathrm{eV/pixel^2}$, with the error given by the fit function. The average energy of the first ring is $c = (0.385 \pm 0.014)\,\mathrm{eV}$. The error is calculated by inserting the upper and lower energy border into the fit function for the first ring. The borders are obtained from the width of the Gaussian distribution

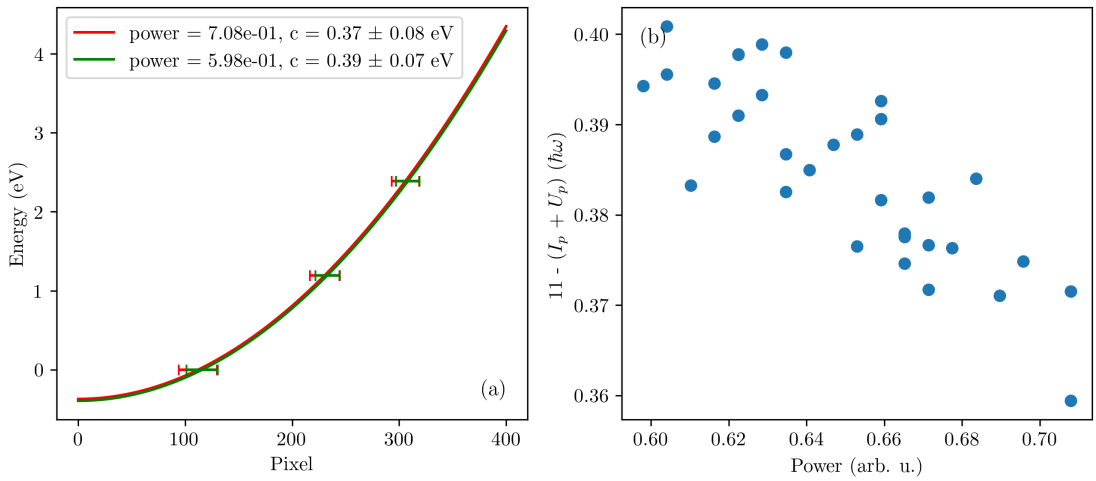

Figure 6.7: (a) Quadratic fit through the ring centers for energy calibration. The pixel positions are mapped to the corresponding energies for the smallest power in green and the highest power in red. The fit result for the offset is displayed in the upper left. (b) Energy of the electrons in the first ring as a function of laser power. The expected linear relation between energy and laser power is observed.

of the first ring. Finally, Fig. 6.4 is calibrated as a function of energy and momentum and presented in Fig. 6.8.

6.4 Theoretical Electron Distribution

In order to evaluate the above-retrieved values, the theoretically expected electron energy distribution has to be computed. Two aspects that directly influence this distribution have to be considered: (i) the ponderomotive shift, which changes the electron energy, and (ii) the photon spectrum, which broadens the distribution. First, the power distribution has to be investigated to calculate the ponderomotive shift. For this, random power values from the whole power distribution are sampled, with a probability given by the power value to the power of the photon number. The pondermotive shift, calculated from the maximum power in Fig. 6.9, is equal to $U_p = 0.77\,\text{eV}$. For an ionization potential of $I_p = 12.13\,\text{eV}$, the energy required for MPI is approximately 12.9 eV. This energy can be reached with 11 photons of the laser used in the present work. Thus, 11 photon MPI is assumed for further calculations, and the exact ionization process will be discussed hereafter. The resulting histogram, which shows the ionization count for every power level, is shown in Fig. 6.9 (a).

This distribution needs to be adjusted for focal averaging to account for the intensity

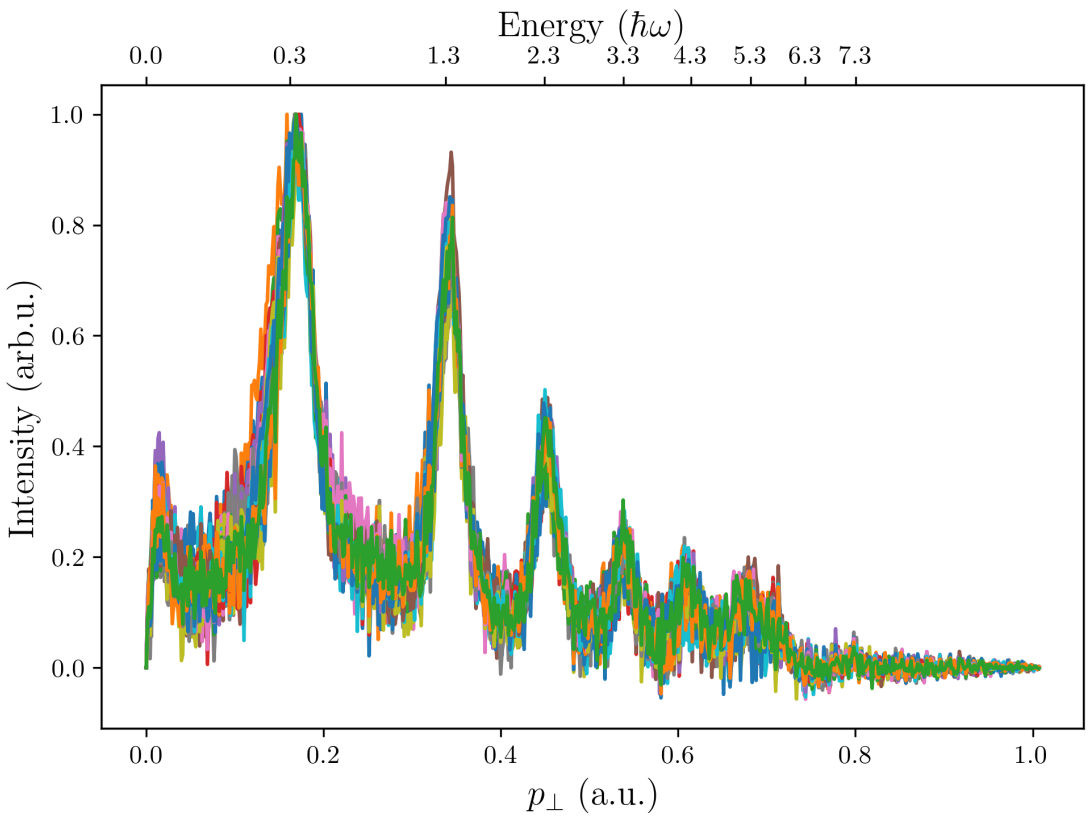

Figure 6.8: Normalized intensity of the VMI image as a function of energy in $\hbar\omega$ and momentum in atomic units. Each color corresponds to the photoelectron spectrum obtained by angular integration of a single detector image.

drop at the edges of the laser focus. The focus is assumed to be of Gaussian shape. Thus, random variables are sampled from a normalized Gaussian shape, and their quadratic value is computed to account for the 2D focus and then multiplied with the power distribution. This shifts the distribution to slightly lower values and broadens it, as shown in Fig. 6.9 (b). The peak power of the laser P_{peak} is calculated from the measured average intra-cavity power P_{avg} by

$$P_{\text{peak}} = \frac{P_{\text{avg}}}{T f_{\text{rep}}}, \tag{6.3}$$

with the pulse FWHM T and the frequency comb repetition rate f_{rep}. This formula is only valid for rectangular pulses and needs to be adjusted for the real pulse shape discussed in the previous chapter. Both shapes are normalized, and the integral over the whole pulse is calculated. The ratio between the integrals yields the factor used for the power rescaling. Then, the distribution of ponderomotive shift for the measured

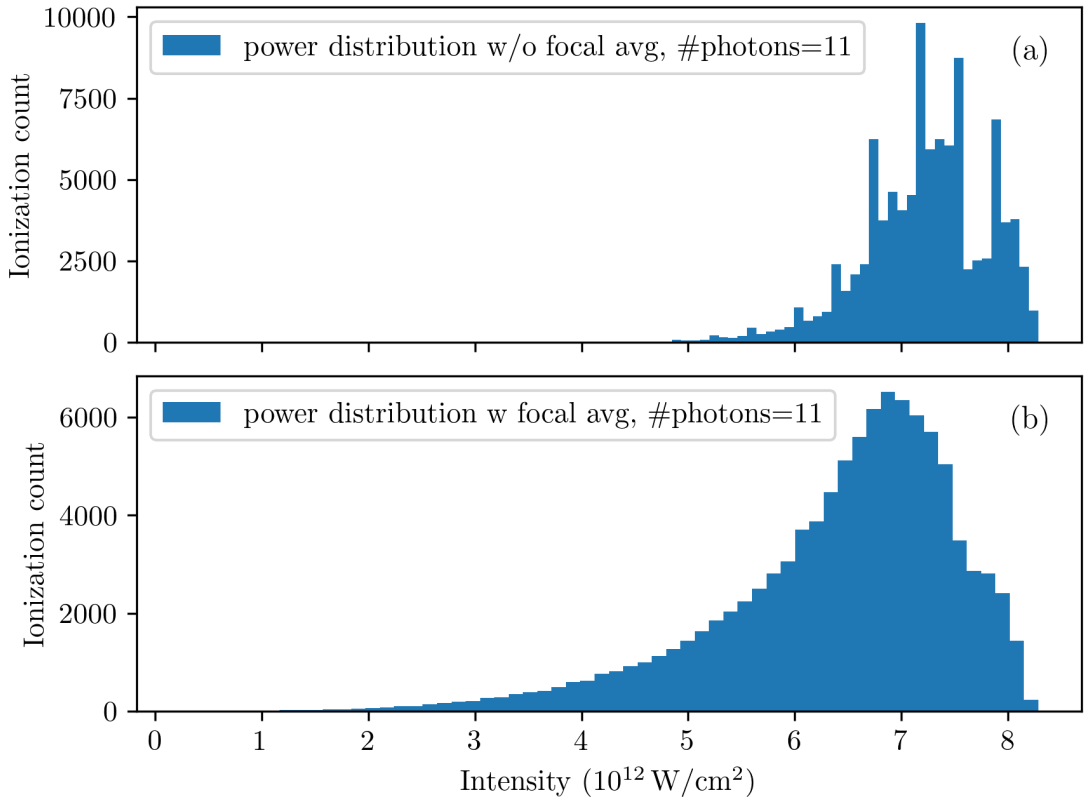

Figure 6.9: Dependence of ionization count on the power distribution. (a) A histogram of the ionization count as a function of the laser power. (b) The same distribution as in (a), but adjusted for focal averaging.

electrons can be estimated directly from the power distribution by calculating the laser intensity and inserting it in Eq. 2.24.

Now the laser spectrum can be taken into account. Due to MPI, random values are sampled 11 times for the photon energies, with the probability distribution given by the laser spectrum. The values are summed up to obtain the energy distribution of the multi-photon process. The resulting distribution is Gaussian, in agreement with the central limit theorem. The Gaussian function fitted to the resulting values (see Fig. 6.10) has a center of $\mu = 13.132\,\text{eV}$ and a width of $\sigma = 0.020\,\text{eV}$. The final electron energy is calculated with Eq. 2.25. The ionization potential and distribution of ponderomotive shift are subtracted from the multi-photon energy spectrum. However, the resulting distribution over the electron energy, shown in Fig. 6.11, does not follow a Gaussian function. Therefore, instead of fitting the values, the electron energy of the first ring is estimated at the maximum of the distribution. This yields an energy of $c = 0.3\,\text{eV}$.

The deviation of the computed from the experimentally measured energy of the

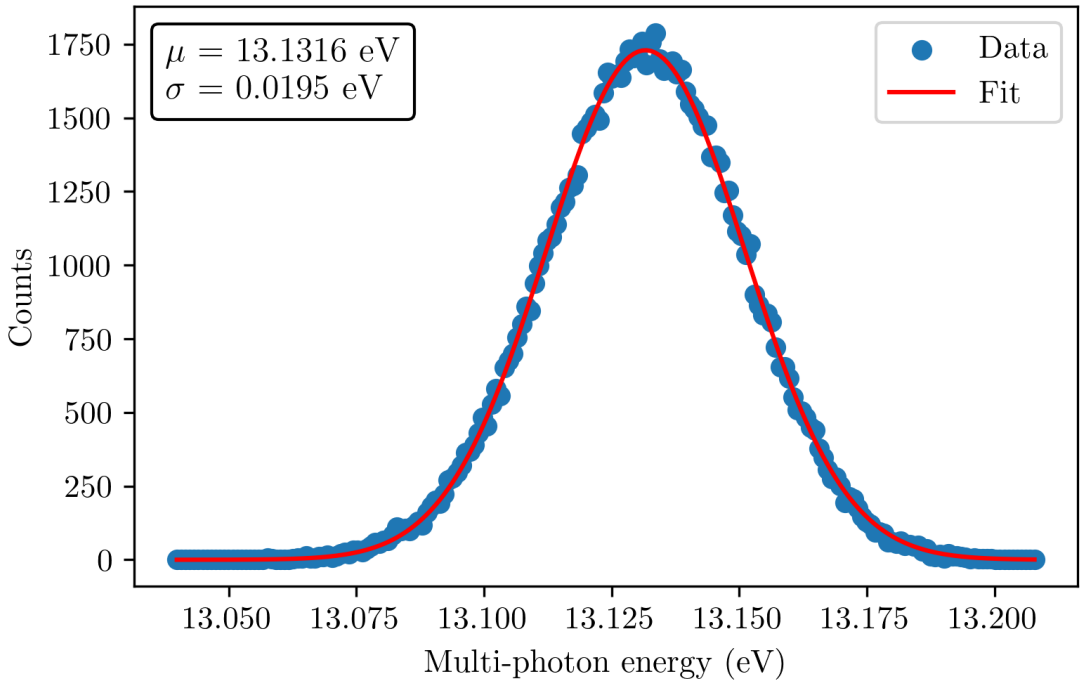

Figure 6.10: Expected energy transfer of 11 photons after MPI. The occurrence is shown as a function of the resulting multi-photon energy. In blue, the calculated data, and in red the fitted Gaussian function is plotted.

first VMI ring is 0.085 eV or 6σ. This means that the theoretical electron energy is underestimated. The most probable explanation is that some effects regarding the laser power are not thought of or that the ionization process proceeds differently. A lower laser power would yield a smaller ponderomotive shift and thus higher electron energy. Another feasible explanation is that the ionization process is simplified in the theoretical calculations by considering 11 photon MPI. Besides, Freeman resonances may take place. To verify this assumption, the excited xenon energy levels are shown in Fig. 6.12. The Rydberg energy levels are shifted ponderomotively due to the laser intensity. In blue, the values are marked, which can be reached with the used laser by 9, 10, or 11 photons. The 4f state can be resonantly excited at a laser intensity of $6.65 \times 10^{12}\,\mathrm{W\,cm^{-2}}$ with 10 photons. Since this intensity is prominently observed in our intensity distribution, as shown in Fig. 6.9 (b), this ionization process is likely. In this case, the expected electron energy is 0.33 eV, which deviates only by 0.055 eV or 3.9σ from the experimentally measured value. The deviations from the experimentally measured value suggest that some effect is not considered during these calculations.

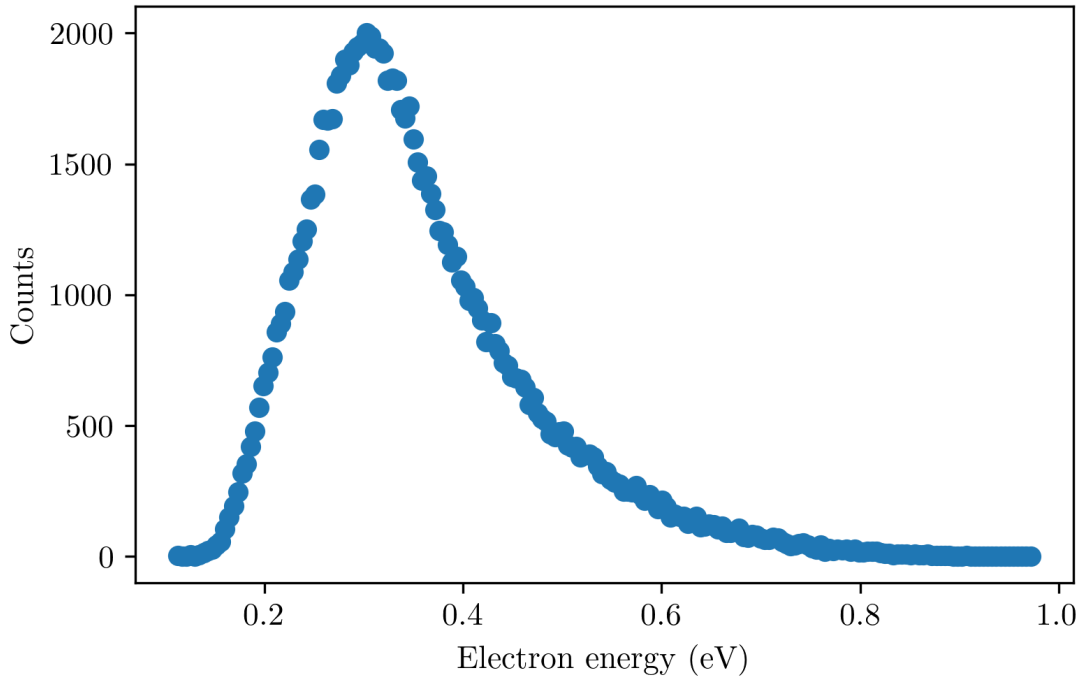

Figure 6.11: Expected electron spectrum after MPI. The ponderomotive shift and ionization potential were subtracted from the expected 11 photon energy spectrum. The number of electrons is shown as a function of the electron energy. The electron energy with the highest occurrence is 0.3 eV.

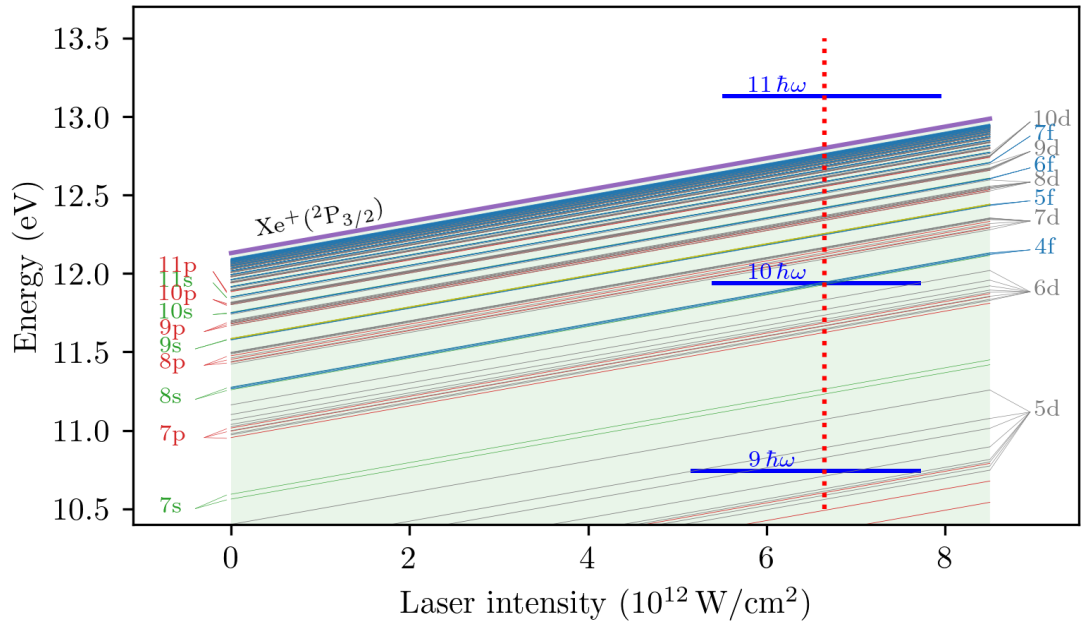

Figure 6.12: Xenon Rydberg levels shifted ponderomotively due to the laser intensity. In purple, the shifted ionization potential is drawn. The blue horizontal lines show the states accessible with 9, 10, or 11 photons at the measured laser power. The dotted red line shows the pathway for the resonant excitation of the 4f state at a laser power of $6.65 \times 10^{12}\,\mathrm{W\,cm^{-2}}$. Adapted from [5].

Chapter 7

Conclusion

In this work, FROG and iFROG were used to characterize the shape of a femtosecond laser pulse. Several noise-reduction algorithms were developed to clean the experimental data. Based on these algorithms, different noise-cleaning protocols were evaluated and optimized. A computational approach was implemented, which allowed the retrieval of iFROG traces using the standard FROG retrieval. The pulse shape was successfully retrieved with a pulse duration of 183 fs. The fluctuations between retrievals were estimated as ±3 fs. The retrieved pulse shape was then used to evaluate experimental VMI data. This data was first cleaned by eliminating artifacts and pixel errors, and then the energy of the photoelectrons was determined. The experimental electron energy distribution was compared with the expected distribution computed using the previously retrieved pulse shape. The electron energy of the first ring in the VMI image was experimentally measured as 0.385(14) eV.

This study demonstrated that the measured FROG image requires good pre-processing to ensure a reliable shape of the retrieved pulse. The significant deviation between the retrieved and measured spectrum hints at an oversimplification of the retrieved temporal pulse shape. Comparison of retrievals obtained using different noise-reduction and symmetrization protocols indicates that the latter is responsible for the oversimplification of the retrieved spectrum. This result suggests that an unambiguous retrieval of the pulse shape requires an experimentally fixed symmetry of the trace and noise reduction.

It was assumed that a crooked delay stage is the reason for the asymmetry in the FROG images. This assumption was tested in an additional experiment by pointing a laser beam directly at the delay stage and measuring the reflection using a camera. The

results of this experiment showed that the angle of the stage changes with the delay. Therefore, the delay stage must be fixed before further measurements are performed.

Faults of the CCD camera are a possible reason for the observed horizontal lines in the measured FROG images. It is assumed that these lines might vanish in repeated measurements. Otherwise, the camera needs to be tested. Another error is the broadening of the trace at zero-delay, which can be caused by reflections in the spectrometer box at high laser intensities. With the above-noted improvements in the experimental setup, it should be possible to achieve a minimum of noise reduction and symmetrization required, which would allow an accurate retrieval of the pulse shape.

The theoretical calculations of the excitation procedure in VMI showed that the ionization does not follow a simple 11 photon MPI since the measured electron energy spectrum does not correspond to the expected energy distribution. Instead, resonant excitation of a Rydberg state of neutral xenon followed by ATI is more likely to occur. The present analysis indicates that the most probable ionization pathway is a ten-photon excitation of the 4f state at $6.65 \times 10^{12}\,\mathrm{W\,cm^{-2}}$ followed by a one-photon ionization. The difference between the electron energy expected from this ionization and the measured one is 0.055 eV or 3.9σ. This suggests that the ionization pathway is more complex than initially supposed. It was previously assumed that the ground state of xenon is not shifted ponderomotively. However, this shift may transfer different states at lower intensities into resonance, which could explain the measured photoelectron energy. Further investigations could be made by (i) stabilizing the cavity power by fixing the locking mechanism and (ii) increasing the resolution of the VMI spectrometer. Moreover, additional measurements at different intensities might help to understand the ionization pathway.

Nevertheless, even without the exact ionization pathway knowledge, the present study demonstrates the functionality of the VMI setup. This setup can thus be applied to the investigation of low-intensity strong-field ionization with VMI and the measurement of the ^{229}Th excited state energy. For the latter, a gating mechanism must be implemented, enabling the selection of electrons emitted after several microseconds delay, given by the decay channel lifetime of 10 µs. The MCP detector could be used for electron measurement. Thorium could be placed on a nano-tip and inserted between the repeller and extractor electrode. Precise measurements of the thorium excited state energy may help advance toward developing a thorium-based nuclear clock.

Acronyms

SPM	Self-Phase Modulation
HWP	Half-Wave Plate
PBS	Polarizing Beam splitter
SHG	Second-Harmonic-Generation
FROG	Frequency Resolved Optical Gating
PSD	Power Spectral Density
iFROG	interferometric Frequency Resolved Optical Gating
MPI	Multiphoton Ionization
ATI	Above-Threshold Ionization
VMI	Velocity Map Imaging
MCP	Microchannel Plate
fsEC	Femtosecond Enhancement Cavity
TOF	Time of Flight
PAD	Photoelectron Angular Distribution

Bibliography

[1] L. Rading, J. Lahl, S. Maclot, *et al.*, "A versatile velocity map ion-electron covariance imaging spectrometer for high-intensity xuv experiments," *Applied Sciences*, vol. 8, no. 6, 2018, ISSN: 2076-3417. DOI: 10.3390/app8060998.

[2] A. T. J. B. Eppink and D. H. Parker, "Velocity map imaging of ions and electrons using electrostatic lenses: Application in photoelectron and photofragment ion imaging of molecular oxygen," *Review of Scientific Instruments*, vol. 68, no. 9, pp. 3477–3484, 1997. DOI: 10.1063/1.1148310.

[3] Y. Huismans, A. Rouzée, A. Gijsbertsen, *et al.*, "Time-resolved holography with photoelectrons," *Science*, vol. 331, no. 6013, pp. 61–64, 2011. DOI: 10.1126/science.1198450.

[4] J. Nauta, J.-H. Oelmann, A. Ackermann, P. Knauer, R. Pappenberger, A. Borodin, I. S. Muhammad, H. Ledwa, T. Pfeifer, and J. R. C. López-Urrutia, "100 mhz frequency comb for low-intensity multi-photon studies: Intra-cavity velocity-map imaging of xenon," *Opt. Lett.*, vol. 45, no. 8, pp. 2156–2159, Apr. 2020. DOI: 10.1364/OL.389327.

[5] J.-H. Oelmann, T. Heldt, L. Guth, J. Nauta, N. Lackmann, V. Wössner, S. Kokh, T. Pfeifer, and J. R. Crespo López-Urrutia, "Photoelectron tomography with an intra-cavity velocity-map imaging spectrometer at 100 mhz repetition rate," *Review of Scientific Instruments*, 2022, submitted.

[6] C. J. Campbell, A. G. Radnaev, A. Kuzmich, V. A. Dzuba, V. V. Flambaum, and A. Derevianko, "Single-ion nuclear clock for metrology at the 19th decimal place," *Phys. Rev. Lett.*, vol. 108, p. 120 802, 12 Mar. 2012. DOI: 10.1103/PhysRevLett.108.120802.

[7] M. Lombardi, T. Heavner, and S. Jefferts, "Nist primary frequency standards and the realization of the si second," en, no. 2, Dec. 2007.

[8] W. Markowitz, R. G. Hall, L. Essen, and J. V. L. Parry, "Frequency of cesium in terms of ephemeris time," *Phys. Rev. Lett.*, vol. 1, pp. 105–107, 3 Aug. 1958. DOI: 10.1103/PhysRevLett.1.105.

[9] K. Beeks, T. Sikorsky, T. Schumm, J. Thielking, M. V. Okhapkin, and E. Peik, "The thorium-229 low-energy isomer and the nuclear clock," *Nature Reviews Physics*, vol. 3, pp. 238–248, 4 Apr. 2021, ISSN: 25225820. DOI: 10.1038/s42254-021-00286-6.

[10] L. V. D. Wense, B. Seiferle, S. Stellmer, J. Weitenberg, G. Kazakov, A. Pálffy, and P. G. Thirolf, "A laser excitation scheme for th 229m," *Physical Review Letters*, vol. 119, 13 Sep. 2017, ISSN: 10797114. DOI: 10.1103/PhysRevLett.119.132503.

[11] B. Seiferle, L. von der Wense, P. V. Bilous, *et al.*, "Energy of the 229th nuclear clock transition," *Nature*, vol. 573, no. 7773, pp. 243–246, Sep. 2019, ISSN: 1476-4687. DOI: 10.1038/s41586-019-1533-4.

[12] M. Morita, "Nuclear Excitation by Electron Transition and Its Application to Uranium 235 Separation," *Progress of Theoretical Physics*, vol. 49, no. 5, pp. 1574–1586, May 1973, ISSN: 0033-068X. DOI: 10.1143/PTP.49.1574.

[13] R. Müller, A. Volotka, S. Fritzsche, and A. Surzhykov, "Theoretical analysis of the electron bridge process in 229th3+," *Nuclear Instruments and Methods in Physics Research Section B: Beam Interactions with Materials and Atoms*, vol. 408, pp. 84–88, 2017, Proceedings of the 18th International Conference on the Physics of Highly Charged Ions (HCI-2016), Kielce, Poland, 11-16 September 2016, ISSN: 0168-583X. DOI: https://doi.org/10.1016/j.nimb.2017.05.004.

[14] P. V. Bilous, H. Bekker, J. C. Berengut, B. Seiferle, L. von der Wense, P. G. Thirolf, T. Pfeifer, J. R. C. López-Urrutia, and A. Pálffy, "Electronic bridge excitation in highly charged ^{229}Th ions," *Phys. Rev. Lett.*, vol. 124, p. 192 502, 19 May 2020. DOI: 10.1103/PhysRevLett.124.192502.

[15] I. Pupeza, C. Zhang, M. Högner, and J. Ye, "Extreme-ultraviolet frequency combs for precision metrology and attosecond science," *Nature Photonics*, vol. 15, no. 3, pp. 175–186, Mar. 2021, ISSN: 1749-4893. DOI: 10.1038/s41566-020-00741-3.

[16] J. Nauta, J.-H. Oelmann, A. Borodin, A. Ackermann, P. Knauer, I. S. Muhammad, R. Pappenberger, T. Pfeifer, and J. R. C. López-Urrutia, "Xuv frequency comb production with an astigmatism-compensated enhancement cavity," *Opt. Express*, vol. 29, no. 2, pp. 2624–2636, Jan. 2021. DOI: 10.1364/OE.414987.

[17] R. Trebino, R. Jafari, S. A. Akturk, P. Bowlan, Z. Guang, P. Zhu, E. Escoto, and G. Steinmeyer, "Highly reliable measurement of ultrashort laser pulses," *Journal of Applied Physics*, vol. 128, p. 171 103, 17 Nov. 2020, ISSN: 0021-8979. DOI: 10.1063/5.0022552.

[18] R. Trebino, K. DeLong, and D. Kane, "Using χ^3 to measure the intensity and phase of an ultrashort laser pulse: Frequency-resolved optical gating," in *Proceedings of LEOS '93*, 1993, pp. 800–801. DOI: 10.1109/LEOS.1993.379435.

[19] I. Amat-Roldán, I. G. Cormack, P. Loza-Alvarez, E. J. Gualda, and D. Artigas, "Ultrashort pulse characterisation with shg collinear-frog," *Opt. Express*, vol. 12, no. 6, pp. 1169–1178, Mar. 2004. DOI: 10.1364/OPEX.12.001169.

[20] J. K. LL.D., "Xl. a new relation between electricity and light: Dielectrified media birefringent," *The London, Edinburgh, and Dublin Philosophical Magazine and Journal of Science*, vol. 50, no. 332, pp. 337–348, 1875. DOI: 10.1080/14786447508641302.

[21] U. Keller, "Ultrafast lasers," 2021.

[22] S. Angstenberger, "Design of a setup for flexible, dispersion-compensated nonlinear femtosecond laser pulse compression adapted to an extreme ultraviolet frequency comb," M.S. thesis, University of Heidelberg, Department of Physics and Astronomy, 2021.

[23] W. Nagourney, *Quantum Electronics for Atomic Physics and Telecommunication: Second Edition*. Oxford University Press, 2014. DOI: 10.1093/acprof:oso/9780199665488.001.0001.

[24] J. Nauta, "An extreme-ultraviolet frequency comb enabling frequency metrology with highly charged ions," Ph.D. dissertation, University of Heidelberg, Combined Faculties of the Natural Sciences and Mathematics, 2020.

[25] V. Wössner, "Tomographische rekonstruktion dreidimensionaler photoelektronenverteilungen mittels intra-cavity velocity map imaging," Bachelor's Thesis, University of Heidelberg, Department of Physics and Astronomy, 2020.

[26] N. Bloembergen, "Nonlinear optics and spectroscopy," *Rev. Mod. Phys.*, vol. 54, pp. 685–695, 3 Jul. 1982. DOI: 10.1103/RevModPhys.54.685.

[27] A. E. Becquerel, "Mémoire sur les effets électriques produits sous l'influence des rayons solaires," *Académie des sciences*, vol. 9, 1839.

[28] A. Einstein, "Über einen die erzeugung und verwandlung des lichtes betreffenden heuristischen gesichtspunkt," *Annalen der Physik*, vol. 322, no. 6, pp. 132–148, 1905. DOI: https://doi.org/10.1002/andp.19053220607.

[29] M. Göppert-Mayer, "Über elementarakte mit zwei quantensprüngen," *Annalen der Physik*, vol. 401, no. 3, pp. 273–294, 1931. DOI: https://doi.org/10.1002/andp.19314010303.

[30] G. Mainfray and G. Manus, "Multiphoton ionization of atoms," *Reports on Progress in Physics*, vol. 54, no. 10, pp. 1333–1372, Oct. 1991. DOI: 10.1088/0034-4885/54/10/002.

[31] R. R. Freeman and P. H. Bucksbaum, "Investigations of above-threshold ionization using subpicosecond laser pulses," *Journal of Physics B: Atomic, Molecular and Optical Physics*, vol. 24, no. 2, pp. 325–347, Jan. 1991. DOI: 10.1088/0953-4075/24/2/004.

[32] R. R. Freeman, P. H. Bucksbaum, H. Milchberg, S. Darack, D. Schumacher, and M. E. Geusic, "Above-threshold ionization with subpicosecond laser pulses," *Phys. Rev. Lett.*, vol. 59, pp. 1092–1095, 10 Sep. 1987. DOI: 10.1103/PhysRevLett.59.1092.

[33] L. V. Keldysh, "Ionization in the Field of a Strong Electromagnetic Wave," *J. Exp. Theor. Phys.*, vol. 20, no. 5, pp. 1307–1314, 1965.

[34] A. Čerki ć and D. B. Milo ševi ć, "Focal averaging and incoherent scattering in laser-assisted radiative recombination and scattering processes," *Phys. Rev. A*, vol. 75, p. 013 412, 1 Jan. 2007. DOI: 10.1103/PhysRevA.75.013412.

[35] "A history of the central limit theorem," in Springer New York Dordrecht Heidelberg London, 2011, ISBN: 978-0-387-87856-0.

[36] W. Yang, M. Springer, J. Strohaber, A. Kolomenski, H. Schuessler, G. Kattawar, and A. Sokolov, "Spectral phase retrieval from interferometric autocorrelation by a combination of graduated optimization and genetic algorithms," *Opt. Express*, vol. 18, no. 14, pp. 15 028–15 038, Jul. 2010. DOI: 10.1364/OE.18.015028.

[37] R. Jafari, T. Jones, and R. Trebino, "100% reliable algorithm for second-harmonic-generation frequency-resolved optical gating," *Opt. Express*, vol. 27, no. 3, pp. 2112–2124, Feb. 2019. DOI: 10.1364/OE.27.002112.

[38] D. Kane, "Real-time measurement of ultrashort laser pulses using principal component generalized projections," *IEEE Journal of Selected Topics in Quantum Electronics*, vol. 4, no. 2, pp. 278–284, 1998. DOI: 10.1109/2944.686733.

[39] P. Sidorenko, O. Lahav, Z. Avnat, and O. Cohen, "Ptychographic reconstruction algorithm for frequency-resolved optical gating: Super-resolution and supreme robustness," *Optica*, vol. 3, no. 12, pp. 1320–1330, Dec. 2016. DOI: 10.1364/OPTICA.3.001320.

[40] G. Stibenz and G. Steinmeyer, "Interferometric frequency-resolved optical gating," *Opt. Express*, vol. 13, no. 7, pp. 2617–2626, Apr. 2005. DOI: 10.1364/OPEX.13.002617.

[41] J. Hyyti, E. Escoto, and G. Steinmeyer, "Pulse retrieval algorithm for interferometric frequency-resolved optical gating based on differential evolution," *Review of Scientific Instruments*, vol. 88, no. 10, p. 103 102, 2017. DOI: 10.1063/1.4991852.

[42] C. Iaconis and I. A. Walmsley, "Spectral phase interferometry for direct electric-field reconstruction of ultrashort optical pulses," *Opt. Lett.*, vol. 23, no. 10, pp. 792–794, May 1998. DOI: 10.1364/OL.23.000792.

[43] M. Miranda, C. L. Arnold, T. Fordell, F. Silva, B. Alonso, R. Weigand, A. L'Huillier, and H. Crespo, "Characterization of broadband few-cycle laser pulses with the d-scan technique," *Opt. Express*, vol. 20, no. 17, pp. 18 732–18 743, Aug. 2012. DOI: 10.1364/OE.20.018732.

[44] N. Abel, "Auflösung einer mechanischen aufgabe.," ger, *Journal für die reine und angewandte Mathematik*, vol. 1, pp. 153–157, 1826.

[45] D. D. Hickstein, S. T. Gibson, R. Yurchak, D. D. Das, and M. Ryazanov, "A direct comparison of high-speed methods for the numerical abel transform," *Review of Scientific Instruments*, vol. 90, no. 6, p. 065 115, 2019. DOI: 10.1063/1.5092635.

[46] "Two-dimensional fourier-based reconstruction methods," in *Computed Tomography: From Photon Statistics to Modern Cone-Beam CT*. Springer Berlin Heidelberg, 2008, ISBN: 978-3-540-39408-2.

[47] S. Kane and J. Squier, "Grism-pair stretcher–compressor system for simultaneous second- and third-order dispersion compensation in chirped-pulse amplification," *J. Opt. Soc. Am. B*, vol. 14, no. 3, pp. 661–665, Mar. 1997. DOI: 10.1364/JOSAB.14.000661.

[48] R. Trebino, K. W. DeLong, D. N. Fittinghoff, J. N. Sweetser, M. A. Krumbügel, B. A. Richman, and D. J. Kane, "Measuring ultrashort laser pulses in the time-frequency domain using frequency-resolved optical gating," *Review of Scientific Instruments*, vol. 68, no. 9, pp. 3277–3295, 1997. DOI: 10.1063/1.1148286.

[49] S. Kleinert, *Pyfrog*, https://github.com/svenkleinert/pyfrog, 2019.

[50] K. DeLong, D. Fittinghoff, and R. Trebino, "Practical issues in ultrashort-laser-pulse measurement using frequency-resolved optical gating," *IEEE Journal of Quantum Electronics*, vol. 32, no. 7, pp. 1253–1264, Jul. 1996, ISSN: 1558-1713. DOI: 10.1109/3.517026.

[51] A. Savitzky and M. J. E. Golay, "Smoothing and differentiation of data by simplified least squares procedures.," *Analytical Chemistry*, vol. 36, no. 8, pp. 1627–1639, 1964. DOI: 10.1021/ac60214a047.

[52] A. V. Nikonov, R. V. Davletshin, N. I. Iakovleva, and P. S. Lazarev, "Savitzky–golay filtering of the spectral sensitivity of photodetector arrays," *Journal of Communications Technology and Electronics*, vol. 62, pp. 1048–1052, 9 Sep. 2017, ISSN: 10642269. DOI: 10.1134/S1064226917090170.

[53] M. Berg, "Tomographic reconstruction of photoelectron momentum distribution obtained through velocity map imaging with a 100 mhz laser in a femtosecond enhancement cavity," Bachelor's Thesis, University of Heidelberg, Department of Physics and Astronomy, 2022.

Aknowledgements

I greatly enjoyed working on this bachelor's thesis at the MPIK.
I would like to thank José Crespo for giving me the opportunity to work in his great group. Further, I would like to thank Laura Cattaneo for being my second examiner.
This thesis would not be possible without the help and supervision of Jan-Hendrik Oelmann, Tobias Heldt, and Lennart Guth. I am very grateful for all the time and support they have given me.
I would like to thank all the members of this group for the enjoyable time and the great cakes.
Finally, I would like to thank my parents for all the support that they have given me.

Erklärung

Ich versichere, dass ich diese Arbeit selbstständig verfasst und keine anderen als die angegebenen Quellen und Hilfsmittel benutzt habe.

Heidelberg, den 17.07.2022,